Computational and experimental studies of reactive intermediates in glycosylation reactions

Remmerswaal, W.A.

Chapter 3

Origin of Facial Selectivity in *C*-Glycosylations of Glucosyl and Mannosyl Cations

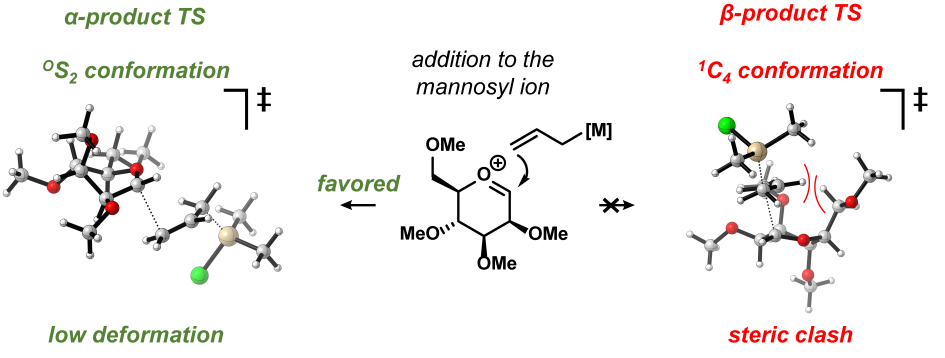

Abstract | Oxocarbenium ions play a central role in shaping the stereochemical outcome of glycosylation reactions. Glycosylations involving $^{4}H_3$-like glycosyl cations often proceed with α-selectivity, while those involving $^{3}H_4$-like glycosyl cations provide the corresponding β-products. This is generally considered to be the result of favorable chair-like transition states. This study reveals that while this analysis holds for addition reaction of various *C*-nucleophiles to the glucosyl cation, addition reactions on the mannosyl cation, which preferentially adopts up a $^{3}H_4$-conformation, proceed with varying stereoselectivity. This can lead to the predominant formation of the α-product, especially when weaker C-nucleophiles are employed. To dissect the mechanisms at play during the addition reactions to the glucosyl and mannosyl oxocarbenium ion conformers, quantum chemical calculations are employed to model the possible S_E2' reactions of a set of allyl nucleophiles leading to both stereoisomers. For the glucosyl cation, the formation of the α-linked products is the result of a bottom-face attack on the $^{4}H_3$ half chair conformer, proceeding through the expected chair-like transition state. For the mannosyl cation however, the favored α-product-forming reactions originate from a higher energy conformer. Notably, the formation of the α-product mannosyl cation is the result of an addition reaction that occurs to a $B_{2,5}$-like conformer through a twist boat-like transition state. The unexpected twist boat-like transition state is favored over a chair-like transition state, because the latter experiences increased steric hindrance between the incoming nucleophile and the pseudo axial ring substituents in a late transition state.

Manuscript in preparation | Remmerswaal, W. A.; Schoenmakers, J.; van Hengst, J. M. A; Hoogers, D.; van Kampen; T.; Hansen, T.; Codée, J.D.C.

Introduction

In synthetic carbohydrate chemistry, the structure of oxocarbenium ions plays a central role in shaping the stereochemical outcome of glycosylation reactions.[1–5] Despite the high reactivity of these intermediates, they can provide striking stereoselectivity.[6–19] The fleeting nature of oxocarbenium ions represents a major challenge in studying these species and determining clear structure-reactivity-stereoselectivity principles. Quantum chemical calculations have provided detailed insight into the stereoelectronic effects of the substituents on the structure, stability and reactivity of these ions.[20–30]

Significant attention has been given to correlating the conformational preferences of oxocarbenium ions with the observed stereoselectivities.[6,13,31] Computational studies have shown that most oxocarbenium ions preferentially adopt $^{3}H_{4}$ or $^{4}H_{3}$-like conformations to accommodate the flat $R_2C{=}O^{+}R$ structure. Nucleophilic attack on either of the half-chair conformers is generally considered to proceed through a chair-like transition state, rather than a twist boat-like transition state.[32] Thus, oxocarbenium ions favoring $^{3}H_{4}$-like conformations are hypothesized to have an 'intrinsic preference' to form the β-product, while those favoring $^{4}H_{3}$-like conformations deliver the α-product. This is commonly referred to as the two-conformer model (Figure 1a).[33] For instance, the glucosyl cation favors a $^{4}H_{3}$ conformations, and therefore its 'intrinsic preference' is formation of the α-product, which is indeed observed in the reaction with allyltrimethylsilane (>98:2, α:β). The mannosyl cation, on the other hand, favors a $^{3}H_{4}$ conformation, which should predominantly provide the β-product, following its associated chair-like transition state. Indeed, in the reaction with triethylsilane-*d,* the β-d-mannoside is the only observed product.[6] However, it has been reported that the addition reaction with allyltrimethylsilane leads to a mixture of products, in which the α-product predominates (66:34 α:β).[34]

This study reports on a study of addition reactions to glucosyl and mannosyl cations to unravel the origin behind these diverging reaction trajectories. For both donors nucleophilicity-stereoselectivity relationships are established, using two *C*-nucleophiles having similar steric requirements but differing in nucleophilicity.[10,35] Using methods described in chapter 2,[32] the addition reactions to the different glycosyl cations are computationally investigated and the possible S_E2' transition states leading to the two possible α and β diastereomers are analyzed. The activation strain model (ASM) was employed to furnish quantitative insight into the electronic factors that impact the different transition states. These studies have shown that, for the mannosyl oxocarbenium ion, the 'two-conformer model' breaks down for the addition reaction of the weak nucleophile: instead of a reaction trajectory that progresses from a $^{3}H_{4}$-like oxocarbenium ion through a $^{3}H_{4}$-$^{1}C_{4}$-like transition state, a pathway that involves attack on a $B_{2,5}$-like oxocarbenium ion and that follows a $^{0}S_{2}$-like transition state appears to be most favorable.

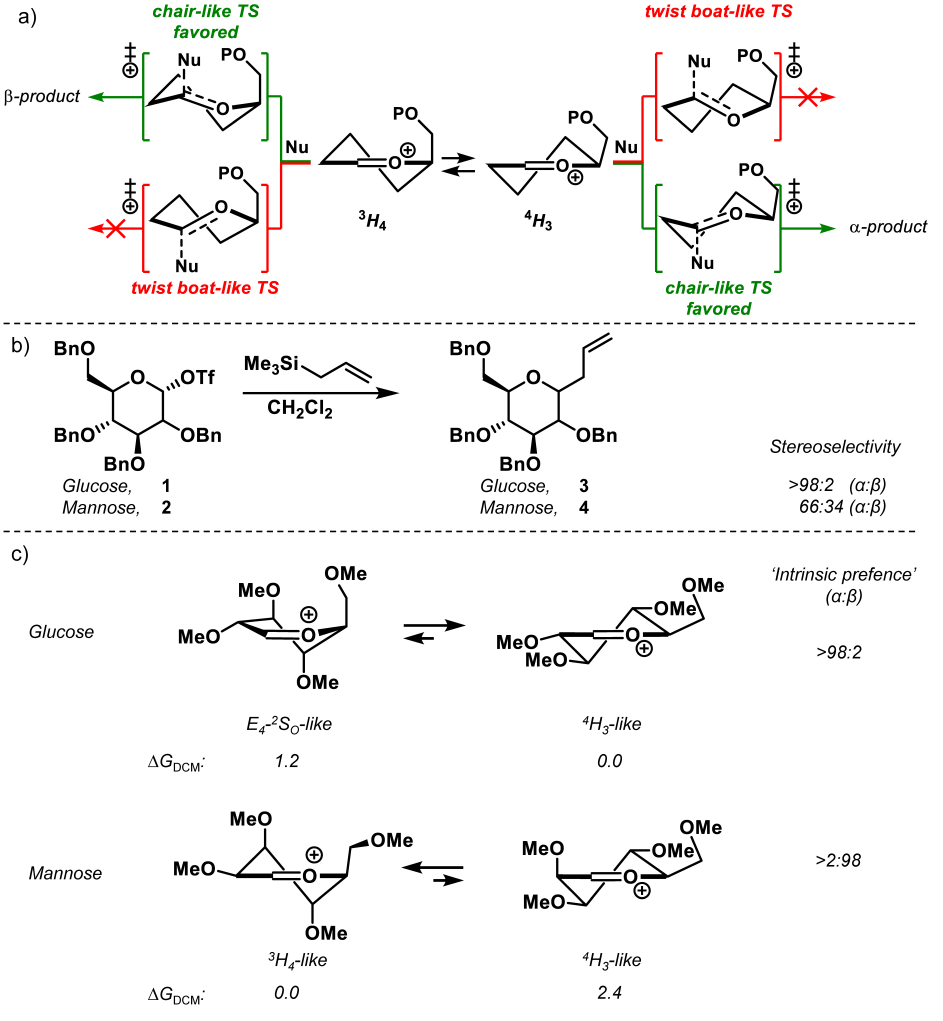

Figure 1. a) The two-conformer model for understanding and predicting the stereoselectivity of glycosyl cations.[13] b) Experimental results for the reaction between 2,3,4,6-tetra-*O*-benzyl-glucosyl/mannosyl triflate and allyltrimethylsilane.[34] c) Computed stability of the 2,3,4,6-tetra-*O*-methyl-glucosyl and mannosyl cation half chair-like conformations, and their calculated 'intrinsic preference', as based on the two-conformer model.[6,32] P = protection group; Nu = nucleophile.

Results and Discussion

To investigate the stereoselectivity of the mannosyl and glucosyl cations, the phenyl 2,3,4,6-tetra-*O*-benzyl-1-thio-glucosyl donor **5** and mannosyl donor **6**[6] were coupled with allyltrimethylsilane using pre-activation conditions, to provide the diastereomeric *C*-allyl products **3** and **4** with similar stereoselectivity as previously reported (glucose donor **5**: >98:2, α:β, mannose donor **6**: 72:28, α:β,). Next, the weaker *C*-nucleophile allyl(chloro)dimethylsilane (as shown by the Mayr nucleophilicity parameter of –0.57[36] as compared to 1.68[37] for allyltrimethylsilane) was used and, while this did not change the stereoselectivity for the reaction with glucosyl donor **5**, the stereoselectivity in the reaction of mannosyl donor **6** shifted, to provide solely the α-product (Scheme 1).

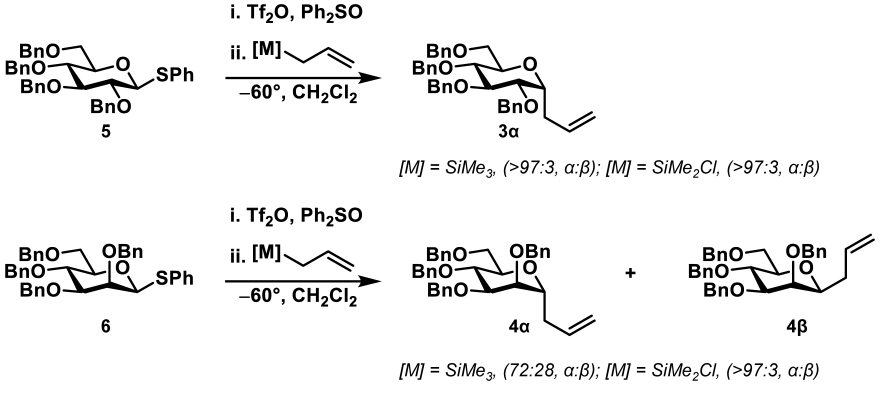

Scheme 1. Glycosylation reactions of per-*O*-benzylated glucose donor **1** and mannose donor **2**, with allyl(chloro)dimethylsilane and allyltrimethylsilane.

To investigate the behavior of the cations in the reactions with the two nucleophiles, the possible S_N1-like reaction paths leading to either the α- or β-product were computationally investigated using the methods developed in chapter 2.[32] In this method the potential energy surface is examined, including various possible S_E2' transition states leading to either the α- or β-product. Importantly, rotation of the C6 substituent was examines, and only the rotamers providing the lowest energy transition states were used in subsequent analyses. To significantly decrease the computational cost, by decreasing the degrees of freedom, benzyl groups were substituted for methyl groups.[6–8,38–40]

For the glucosyl and mannosyl cations, an extensive screening of possible reaction trajectories revealed six transition states (Figure 2). Three α-product-forming pathways were found: the expected bottom-face attack on a $^4H_3$-like conformer that passes through a $^4C_1$-shaped transition state, a bottom-face attack on a $^3H_4$-like conformer that passes through a $^3S_1$-like transition state, and a transition state was found for a trajectory that involves bottom-face attack on a $B_{2,5}$-like conformer leading to a $^OS_2$-like transition state.[41] In addition, three possible β-product-forming pathways were identified: a top-face attack on a $^3H_4$-conformer that passes through a $^1C_4$-shaped transition state, top-face attack on a $^4H_3$-like conformer through a $^1S_3$-shaped transition state, and a top-face attack on a $B_{2,5}$-conformer through a $^1S_5$-shaped transition state. Bottom-face additions to the $^3H_4$-like conformers were unfavorable, and, during transition state searches, the glycosyl cations deformed to other conformers in going to the transition states. Structures of all transition states can be found in Figure 2, while geometries and energies of all stationary points (including products) can be found in Tables S1 and S2.

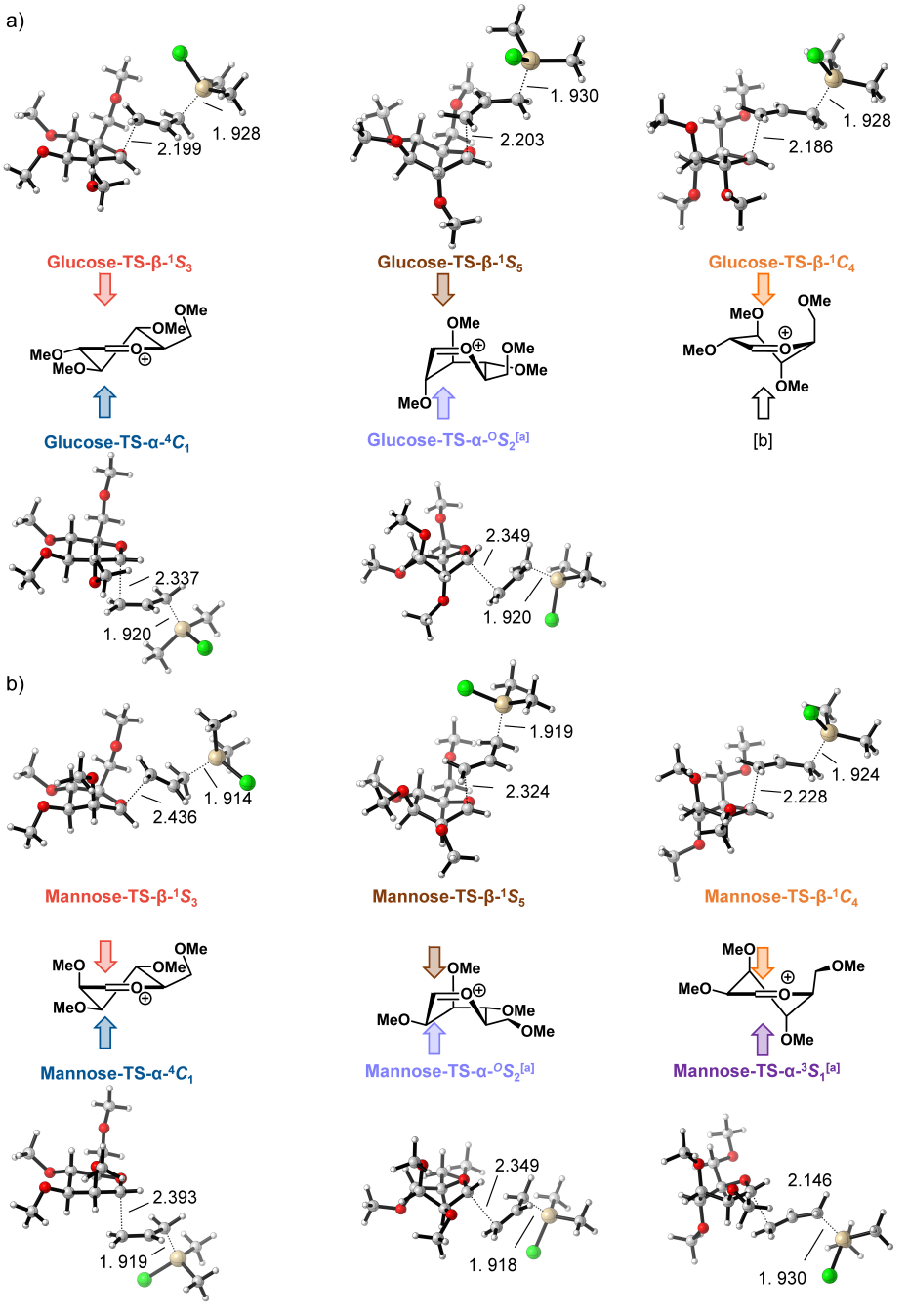

Figure 2. Structures[42] of the transition states of the S_E2' reactions of ally(chloro)dimethylsilane and the glucosyl (a) or mannosyl (b) cations. Key distances are given in Å. [a] A representative structure for the transition state geometry was used.[41] [b] The bottom-side attack on the $^{3}H_{4}$ yields is unfavorable, instead the glycosyl cations deform to other transition state shapes during searches.

The potential energy surface for the S_E2' additions of allyl(chloro)dimethylsilane to the glucosyl cation are shown in Figure 3.[43] As previously reported,[6] the overall lowest energy conformation for the glycosyl cation is the $^4H_3$ half chair, with its higher energy counterpart on the other side of the Cremer–Pople sphere adopting a skewed E_4-$^2S_0$ conformation (1.2 kcal mol^{-1}). As described above, five plausible transition states were found for the addition reaction of allyl(chloro)dimethylsilane: three leading to the formation of the β-product and two that lead to the α-allyl glucoside. While the chair-shaped TSs are generally considered to be the most important, the computations reveal this is not necessarily true in all cases. Notably, during the β-product-forming pathways, this transition state has the highest activation energy (TS-β-$^1C_4$, 15.2 kcal mol^{-1}), with the two boat-type transition states being more favorable (TS-β-$^1S_5$, 14.3 kcal mol^{-1} and TS-β-$^1S_3$, 12.8 kcal mol^{-1}). Thus, the top-face attack on the $^4H_3$ conformation (TS-β-$^1S_3$) was the lowest energy β-product-forming pathway, and is –2.5 kcal mol^{-1} more favorable than TS-β-$^1C_4$. These results stand in contrast to those of mono-substituted pyranosyl cations, where the twist boat-like transition states were found to be much higher in energy. Likely, this outcome is the result of more unfavorable interactions between the nucleophile and the electrophile, as well as between substituents on the glycosyl ring as the nucleophile approaches the densely functionalized glucosyl cation. In addition, the transition state for the addition reactions to the glucosyl cation are earlier than those for the addition reactions to the mono-substituted cations. This can be seen from a much longer C_1–C_{allyl} distance in the TS-β-$^1S_3$ for the glucosyl cation (2.199 Å), compared to, for example, the mono-substituted C-5 CH_2OMe cation (2.049 Å). The greater distance between the glucosyl cation and the nucleophile, results in less conformational change and therefore the conformational penalty for the glucosyl cation is relatively small as compared to that for the stripped glycosides, undergoing a similar addition (Supplementary Figure S5). Thus, the stronger steric interactions of the nucleophile in the axial rich TS-β-$^1C_4$, in combination with the relatively small conformational penalty for TS-β-$^1S_3$, that originates from an oxocarbenium ion conformer (*i.e.*, the $^4H_3$-conformer) that is significantly lower in energy than its counterpart (the $E_4/^2S_0$ conformer) may render the top-face addition to the $^4H_3$ conformer the most favorable β-product-forming pathway. These results indicate that twist boat or boat-like transition states should not *a priori* be ruled out.

Next, the two α-product-forming pathways involving the glucosyl cation were examined. The TS-α-$^4C_1$ (11.2 kcal mol^{-1}) was significantly lower than the TS-α-$^0S_2$ (13.5 kcal mol^{-1}). Likely this difference in barrier height is the result of the low ground state energy of the $^4H_3$-conformer alongside the relatively minor destabilizing interactions that develop upon attack on the α-face of this ion. Overall, TS-α-$^4C_1$ is the most favorable transition state, being –1.6 kcal mol^{-1} more favorable than the lowest energy transition state leading to the β-product (TS-β-$^1S_3$), matching the experimentally obtained stereoselectivity

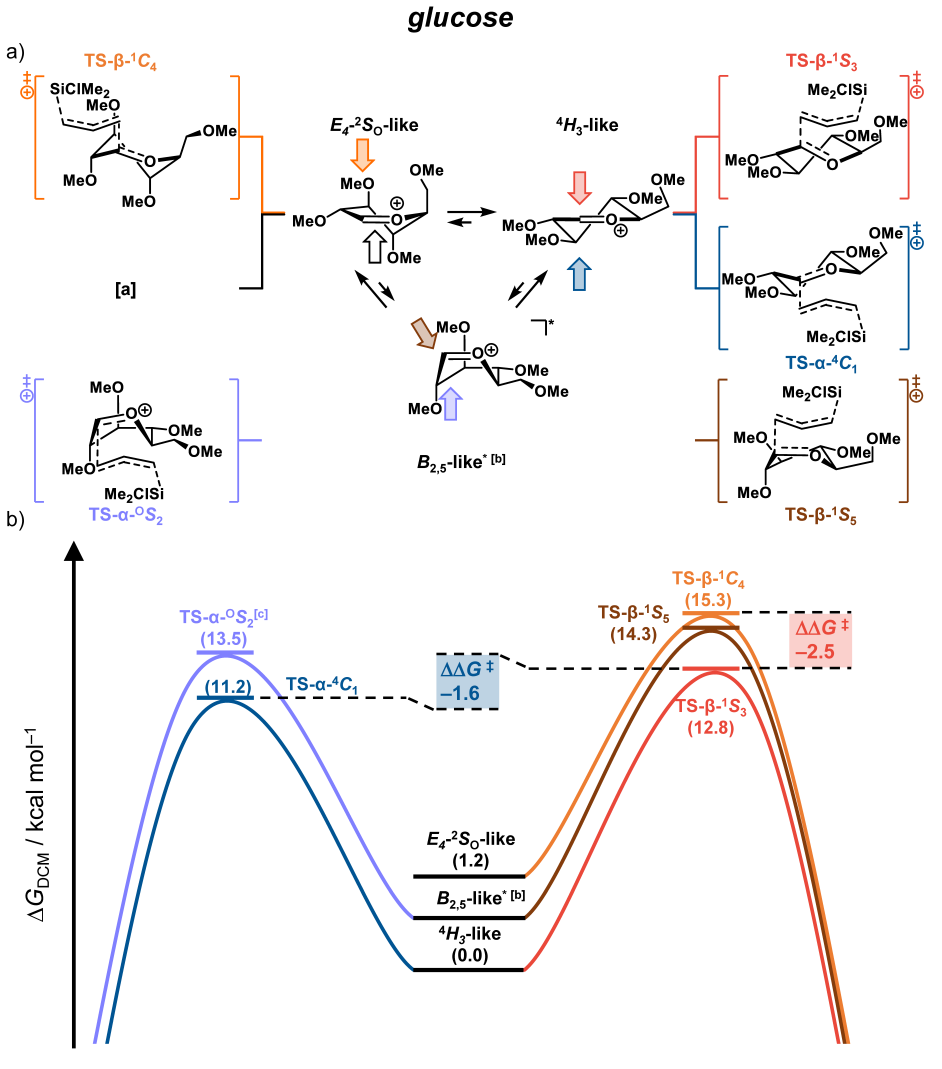

Figure 3. The possible S_E2' reaction pathways (a) and the corresponding reaction profiles (b) of the addition of allyl(chloro)dimethylsilane to the glucosyl cation via the following transition states: TS-β-$^1C_4$ (orange), TS-β-$^1S_5$ (brown), TS-β-$^1S_3$ (red), TS-α-$^OS_2$ (light blue) and TS-α-$^4C_1$ (blue). Energies are depicted as Gibbs free energies (T = 213.15 K) and were computed at PCM(CH_2Cl_2)-B3LYP/6-311G(d,p). [a] The TS-α-$^3S_1$ is unfavorable and could not be located. [b] The itinerary leading up to TS-α-$^OS_2$ and TS-β-$^1S_5$ start from a boat-like non-stationary point. [c] A representative structure for the transition state geometry was used.[41]

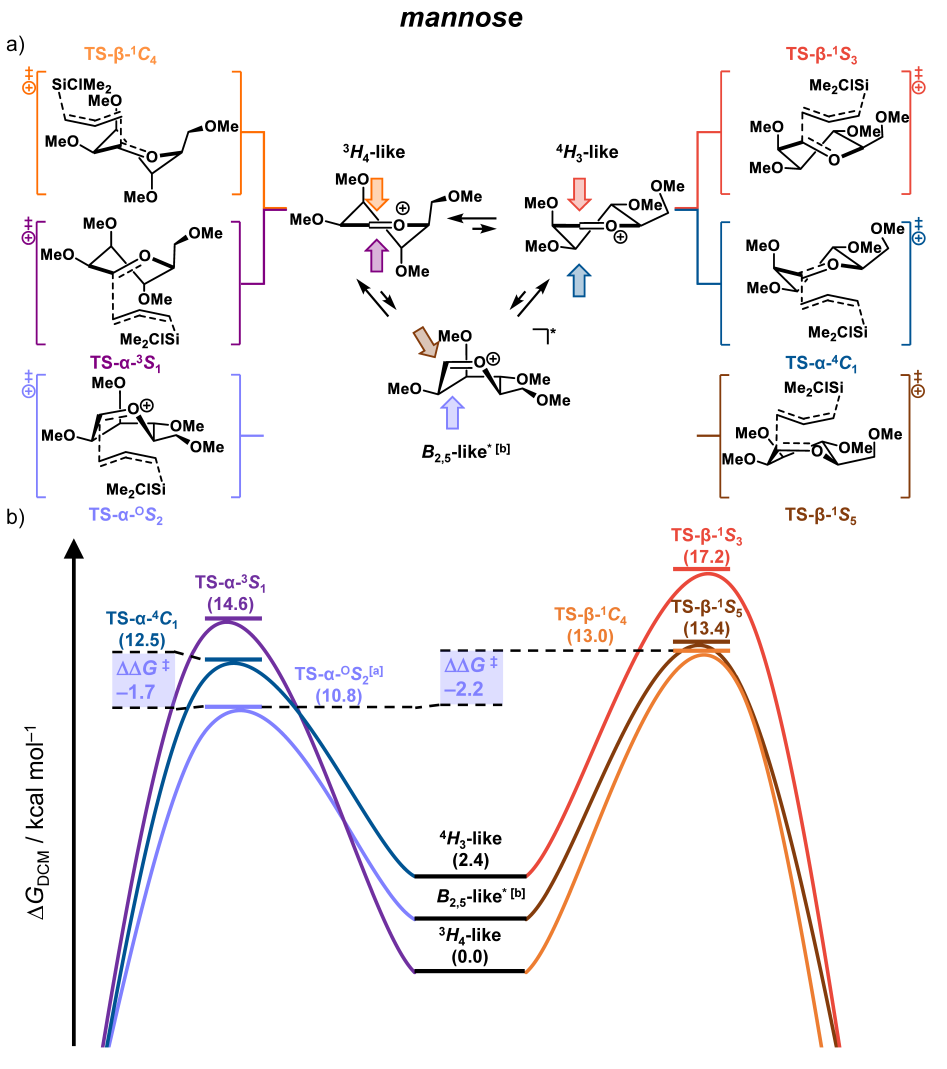

Figure 4. The possible S_E2' reaction pathways (a) and the corresponding reaction profiles (b) of the addition of allyl(chloro)dimethylsilane to the mannosyl cation via the following transition states: TS-β-$^1C_4$ (orange), TS-β-$^1S_5$ (brown), TS-β-$^1S_3$ (red), TS-α-$^OS_2$ (light blue), TS-α-$^3S_1$ (purple), and TS-α-$^4C_1$ (blue). Energies are depicted as Gibbs free energies (T = 213.15 K) and were computed at PCM(CH_2Cl_2)-B3LYP/6-311G(d,p). [a] A representative structure for the transition state geometry was used.[41] [b] The itinerary leading up to TS-α-$^OS_2$ and TS-β-$^1S_5$ start from a boat-like non-stationary point.

The S_E2' additions of allyl(chloro)dimethylsilane to the mannosyl cation were then examined (Figure 4). The mannosyl cation preferentially adopts a $^3H_4$ half chair structure, and the $^4H_3$ half chair is significantly higher in energy (2.4 kcal mol^{-1}). First, the three β-product-forming pathways of the mannosyl cation were analyzed. As expected, the top-face attack on a $^4H_3$ passing through TS-β-$^1S_3$ is unfavorable (17.2 kcal mol^{-1}). The alternative β-product-forming transition state TS-β-$^1C_4$, originating from the $^3H_4$ half chair, was significantly more favorable (13.0 kcal mol^{-1}). Notably, top-face attack of the $B_{2,5}$ was also found to be relatively favorable (TS-β-$^1S_5$, 13.4 kcal mol^{-1}). Subsequently, three α-product-forming pathways were examined. As expected, the TS-α-$^3S_1$-like transition state was very unfavorable (14.6 kcal mol^{-1}). Remarkably, it appeared that kcal mol^{-1}), but rather the bottom-face attack on the $B_{2,5}$ conformer (TS-α-$^0S_2$, 10.8 kcal mol^{-1}), which is favored by –1.7, the most favorable α-product-forming pathway is the result of a bottom-face approach on the $^4H_3$ conformation (TS-α-$^4C_1$, 12.5 kcal mol^{-1} with respect to TS-α-$^4C_1$. This mode of attack has the lowest overall barrier, being favored by –2.2 kcal mol^{-1} over the TS-β-$^1C_4$. This favorable reaction itinerary accounts for the preference of allyl(chloro)dimethylsilane to attack the mannosyl cation in an α-selective manner and represents a notable deviation from the 'two-conformer model'.

The reaction profiles of the reactions with allyltrimethylsilane were then examined. It was observed that the relative order of the transition states was not altered as a result of the increased nucleophilicity of allyltrimethylsilane with respect to allyl(chloro)dimethylsilane. Thus, the most favored α- and β-product-forming pathways for allyl(chloro)dimethylsilane are also the favored approaches for allyltrimethylsilane. Structures of the transition state, the accompanying reaction profiles, and the potential energy surfaces of each addition for allyltrimethylsilane can be found in Supplementary Figures S6-S10. It is noted that the difference between the α- and β-product-forming pathways slightly decreases going from allyl(chloro)dimethylallyl to allyltrimethylsilane. While for allyl(chloro)dimethylsilane the α-product-forming pathways are favored by –1.6 and –2.2 kcal mol^{-1} for, respectively, the glucosyl and mannosyl cation, for allyltrimethylsilane the α-product-forming pathways are favored by –1.1 and –1.8 kcal mol^{-1}, respectively. A difference in absolute barrier height was also noted. Regardless of the glycosyl cation, the barrier heights of all transition states diminish in energy (∼ –2-3 kcal mol^{-1}) as the nucleophilicity increases. This decrease of the activation energy is likely related to a smaller HOMO–LUMO gap for the reactions with allyltrimethylsilane, as a result of having a better leaving group.[44]

To gain quantitative insight into the physical factors affecting the relative barrier height of the transition states discussed above, the activation strain model (ASM) of reactivity was employed for the reactions with allyl(chloro)dimethylsilane.[45–48] The ASM is a fragment-based approach in which the potential energy surface can be described with respect to, and understood in terms of, the characteristics of the reactants, *i.e.*, the allylic nucleophile and the glycosyl oxocarbenium ion substrate (see method section for more details). Here, the ASM decomposes the total electronic energy (ΔE_{DCM}, in diagrams shown as ΔE) into strain energy (ΔE_{strain}) and interaction energy (ΔE_{int}). The strain energy is the destabilizing energy resulting from deformation of the individual fragments, and the interaction energy is the (usually stabilizing) interaction between the fragments. In the presented activation strain diagrams (ASDs), the intrinsic reaction coordinate (IRC) is projected onto the carbon–leaving group (C•••Si) stretch of the nucleophile and the distance between the carbon atom of the nucleophilic allyl and C1 (C_1•••C_{allyl}). These critical reaction coordinates undergo well-defined changes during the reaction from the reactants via the transition state to the product and have been shown to be a valid reaction coordinate for studying bimolecular reactions. Energy decomposition analysis (EDA) was applied to the ΔE_{int} term to decompose the gas phase electronic energy into electrostatic interactions (ΔV_{elstat}), Pauli repulsion (ΔE_{Pauli}) and orbital interaction energy (ΔE_{oi}). The EDA energies depicted are gas phase electronic energies (ΔE_{gas}).[49]

To understand the origin of the facial selectivity of the glucosyl cation, the α and β-product-forming pathways were compared. Figure 5a and b show the ASDs and EDAs for the most favorable α and β-product-forming transition states (TS-α-$^4C_1$ and TS-β-$^1S_3$) along the reaction coordinate projected on the C•••Si stretch. The glucosyl TS-α-$^4C_1$ pathway is more favorable than the glucosyl TS-β-$^1S_3$ due to more stabilizing interaction energy, which can be seen from the blue dotted line lying under the red dotted line (Figure 5a). To gain understanding into the physical factors resulting in this difference in interaction energies, EDA was applied. When the IRC is projected at the C•••Si stretch (Figure 5b), it can be seen that Pauli repulsion is responsible for the difference in interaction energy. The central role of the Pauli repulsion in this analysis is the result of the allyl being much closer (at the same C•••Si stretch) to the anomeric center of the glycosyl cation in the TS-β-$^1S_3$ pathway than the TS-α-$^4C_1$ itinerary. This dependence of EDA on the nucleophile•••electrophile has been previously noted,[50,51] and thus for a more insightful comparison of the interaction energy it can be performed at a similar C_1•••C_{allyl} bond distance and for consistency, here all ASMs

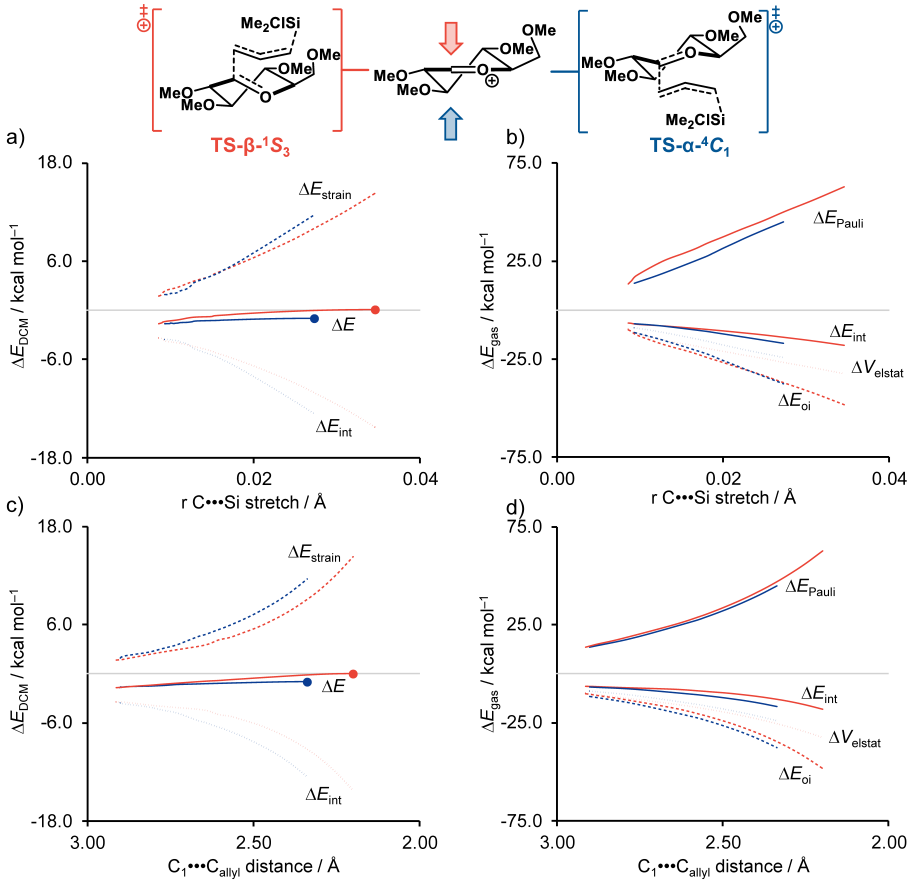

Figure 5. Activation strain (a and c) and energy decomposition analysis (b and d) for the S_E2' reactions of allyl(chloro)dimethylsilane + glucosyl cation via the α-product-forming TS-α-$^4C_1$ (blue) and via the β-product-forming TS-β-$^1S_3$ (red). Energy values are plotted to the transition state (indicated by a dot), along the IRC projected on the C•••Si bond stretch (a and b) or C_1•••C_{allyl} bond distance (c and d). Energies are depicted as electronic energies and were computed at PCM(CH_2Cl_2)-B3LYP/6-311G(d,p) for ΔE_{DCM} or ZORA-B3LYP/TZ2P//PCM(CH_2Cl_2)-B3LYP/6-311G(d,p) for ΔE_{gas}.

and EDAs are examined using the IRC projected on the C•••Si stretch as well as the C_1•••C_{allyl} bond distance.[52] In Figure 5c it is shown that TS-α-$^4C_1$ proceeds with more interaction energy at a similar C_1•••C_{allyl} bond distance. When Figure 5d is examined, it becomes apparent that the Pauli repulsion is not the main contributor to the difference in interaction energy. Instead, the difference in orbital interaction energy has the most influence.[52,53] Analysis of the LUMO energy of the glycosyl cation in both pathways (Supplementary Figure S11), shows that the LUMO of the oxocarbenium ion decreases more steeply when following the pathway towards the TS-α-$^4C_1$ than when the TS-β-$^1S_3$ pathway is followed. This lower LUMO energy in the TS-α-$^4C_1$ is the result of an advanced degree of pyramidalization (rehybridization), leading to a better HOMO-LUMO interaction and, thus, more stabilizing orbital interaction energy. This favorable LUMO energy of the chair-like transition state is in line with the results of the in chapter 2 studied mono-substituted pyranosyl rings:[32] deformation of the half chair to a chair-like transition state is easier compared to the deformation to a twist boat-like transition state because no eclipsing interactions develop, allowing for more pyramidalization and a steeper drop of the LUMO energy along the reaction path.[32]

Next, the unusual itinerary of the β-product-forming pathway was examined. Generally, this twist boat-like transition state shape (TS-β-$^1S_3$) is ruled out beforehand, assuming a chair-like transition state to be the most favorable (Figure 1a). Although this postulation holds for the tetrahydropyran oxocarbenium Ions,[32] for the fully decorated glycosyl cations, the twist boat-like transition state shape can be more favorable (Figure 3). Although the β-product is not formed in this reaction (Scheme 1), understanding this breakdown of the two-conformer model may be relevant for the development of more comprehensive models. Therefore, ASM was applied to understand why top face attack on the $^4H_3$-like conformation, which proceeds via a twist boat-like transition state, is more favorable than the top face attack on the $^3H_4$-like conformation through a chair-like transition state. Figure 6a and b show the ASDs of the TS-β-$^1C_4$ (orange) *versus* the TS-β-$^1S_3$ (red) for the glucosyl cation (the corresponding EDA can be found in Supplementary Figure S12). As described above, it was found that the TS-β-$^1S_3$ is preferred over the TS-β-$^1C_4$. This preference is dictated by the strain, as can be seen from Figure 6a and b, which shows that the ΔE_{strain} for the pathway proceeding through TS-β-$^1S_3$ is significantly lower than the ΔE_{strain} for the alternative path along the reaction coordinate, as defined by either the C•••Si stretch (Figure 6a) or the C_1•••C_{allyl} bond distance (Figure 6b). The strain can be almost completely attributed to the strain of the glycosyl cation (as there is little difference in the strain of the allyl nucleophile, see supplementary Figure S13a and b) and the difference in strain is already present at the start of ASD. It can thus be derived that the origin of the higher strain lies in 'starting' from an energetically higher conformer (the $^3H_4$-like conformer). While it is more favorable to deform a half-chair-like conformer to a chair-like conformer, as can be seen from the two strain curves converging along the reaction coordinate, this deformation is not enough for the TS-β-$^1C_4$ pathway to approach the TS-β-$^1S_3$ path energy-wise. Overall, it appears that the conformational preference of the glycosyl cation dictates the shape of the β-product-forming transition state.

To summarize, the preference for the α-glucosyl product-forming pathway, passing through a chair-like transition state, is the result of the conformational preference of the glycosyl cation for the $^4H_3$ conformation, in combination with a favorable pathway for nucleophilic attack. The high energy of the alternative $^3H_4$-like conformer disfavors a reaction on this intermediate and the computational studies have revealed that a top-face approach on the $^4H_3$ conformation, that leads to a trajectory having a twist boat-like transition state (TS-β-$^1S_3$), is more favorable than top-face attack on the $^3H_4$ conformer that proceeds via a chair-like transition state (TS-β-$^1C_4$). The top-face attack pathway that leads to TS-β-$^1S_3$ is considerably less favorable than the bottom face attack on the $^4H_3$ conformer. The more favorable orbital interaction and to a lesser extend diminished Pauli repulsion render this α-product-forming pathway towards the chair-like transition state the most favorable for the glucosyl oxocarbenium ion.

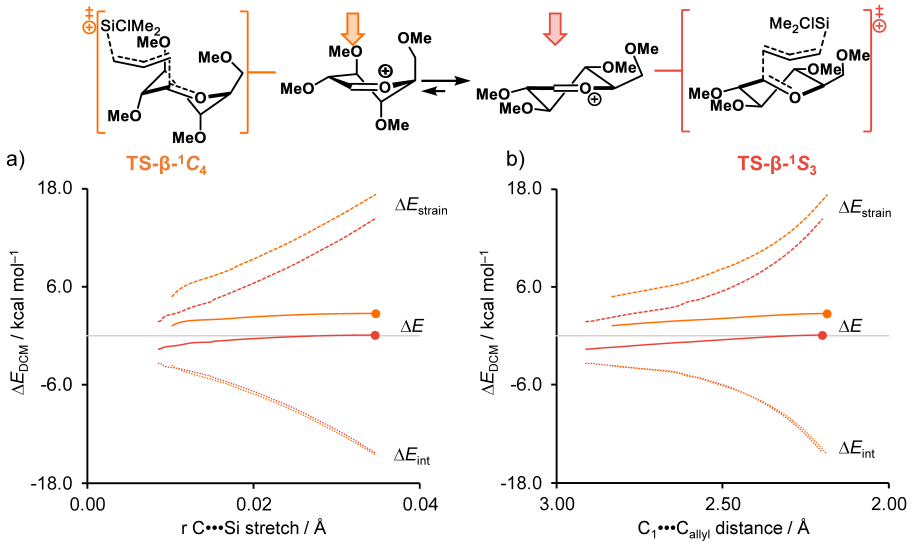

Figure 6. Activation strain analysis for the S_E2' reactions of allyl(chloro)dimethylsilane + glucosyl cation via the β-product-forming TS-β-$^1C_4$ (orange) and via the β-product-forming TS-β-$^1S_3$ (red), where the energy values are plotted to the transition state (indicated by a dot), along the IRC projected on the C•••Si bond stretch (a) or C_1•••C_{allyl} bond distance (b). Energies are depicted as electronic energies and were computed at PCM(CH_2Cl_2)-B3LYP/6-311G(d,p) for ΔE_{DCM}. [a] The TS-α-$^0S_2$ pathway was plotted against the constrained potential energy surface.[41]

To discern the physical factors responsible for the α-selective nature of the mannosyl cation (Scheme 1 and Figure 4), the favored pathways leading to the α-mannosyl (TS-α-$^0S_2$) and β-mannosyl (TS-β-$^1C_4$) products were compared. The ASD using the C•••Si bond stretch to describe the reaction coordinate (Figure 7a) shows that the pathway leading to TS-α-$^0S_2$ is more favorable than the pathway towards TS-β-$^1C_4$ because of less destabilizing strain and more favorable interaction energy. The differences in strain parallel the results of the mono-substituted C5-CH_2OMe system examined in chapter 2.[32] The TS-β-$^1C_4$ pathway starts out with less strain, resulting from the addition to a more stable ($^3H_4$-like) conformer. However, the strain increases more steeply than in the alternative TS-α-$^0S_2$ pathway. This difference in strain energy is caused by the deformation of the $^3H_4$ conformer to accommodate the interaction with the incoming nucleophile ("absorbing" the developing steric repulsion, *vide infra*).[54] Next, the differences in interaction energy were investigated. In Figure 7c, it can be observed that at the same C_1•••C_{allyl} bond distance, the interaction energy in the TS-α-$^0S_2$ pathway is lower all along the reaction path.

To understand the factors involved in this lower interaction energy, EDA was applied. It was observed that the main differences in interaction energy are the result of increased destabilizing Pauli repulsion in the TS-β-$^1C_4$ pathway, which is consistent along the C_1•••C_{allyl} bond distance (Figure 7d).[52,55] The increased Pauli repulsion building up in the TS-β-$^1C_4$ pathway can be easily understood as steric repulsion between the incoming nucleophile and the *pseudo*-axial substituents at C3 and C5. Thus, while the mannosyl cation prefers to adopt a $^3H_4$-like conformation, reactions with a weak nucleophile require a relatively late transition state, at which point significant deformation of the favorable $^3H_4$-like conformation has to take place to accommodate the interactions with the nucleophile. As a result, reactions taking place on a higher energy intermediate, the $B_{2,5}$-like conformer, can become more favorable. The earlier transition state in reactions of this cation requires less deformation and involves less Pauli repulsion.

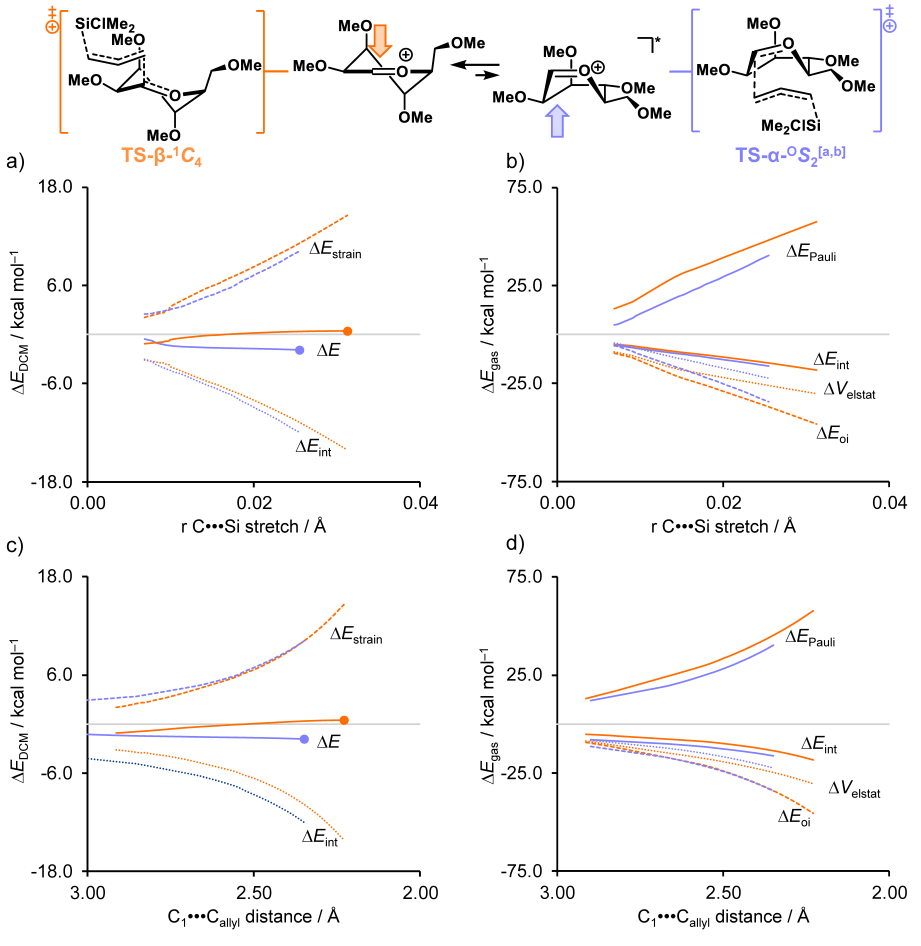

Figure 7. Activation strain (a and c) and energy decomposition analysis (b and d) for the S_E2' reactions of allyl(chloro)dimethylsilane + mannosyl cation via the α-product-forming TS-α-$^OS_2$ (light blue) and via the β-product-forming TS-β-$^1C_4$ (orange). Energy values are plotted to the transition state (indicated by a dot), along the IRC projected on the C•••Si bond stretch (a and b) or C_1•••C_{allyl} bond distance (c and d). Schematic representation of the physical factors influencing the facial selectivity of the mannosyl cation (d). Energies are depicted as electronic energies and were computed at PCM(CH_2Cl_2)-B3LYP/6-311G(d,p) for ΔE_{DCM} or ZORA-B3LYP/TZ2P//PCM(CH_2Cl_2)-B3LYP/6-311G(d,p) for ΔE_{gas}. [a] The TS-α-$^OS_2$ pathway was plotted against the constrained potential energy surface.[41] [b] The itinerary leading up to TS-α-$^OS_2$ starts from a boat-like non-stationary point.

Finally, it was examined why the bottom-face attack on a boat-like conformation leading to TS-α-$^{0}S_{2}$ is more favorable than the canonical bottom-face attack on a half chair-like conformation (TS-α-$^{4}C_{1}$). The ASM analyses are depicted in Figure 8, which show the ASDs for the TS-α-$^{4}C_{1}$ (blue) *versus* the TS-α-$^{0}S_{2}$ (light blue) pathways for the mannosyl cation. From the C•••Si bond stretch diagram (Figure 8a), it can be seen that both bottom face pathways incur similar strain, while the approach leading to TS-α-$^{4}C_{1}$ is paired with less stabilizing interaction energy. As mentioned previously, since the C•••Si bond stretch and C_1•••C_{allyl} bond distance do not always develop parallel in all the reaction paths, the EDA was also plotted at a similar C_1•••C_{allyl} bond distance. It can be seen from projecting the IRC on the C_1•••C_{allyl} bond distance that the interaction energy of the TS-α-$^{0}S_{2}$ pathway is indeed lower at a similar C_1•••C_{allyl} bond distance (Figure 8c). At a similar C_1•••C_{allyl} bond distance, the TS-α-$^{4}C_{1}$ develops much more strain resulting from the cation (Supplementary Figure S13c and d). This difference in strain, is the result of the TS-α-$^{4}C_{1}$ starting from an energetically higher $^{4}H_{3}$ conformer, while the TS-α-$^{0}S_{2}$ pathway starts from the more stable $B_{2,5}$-like conformation. The corresponding EDA at the same C_1•••C_{allyl} bond distance (Figure 8d) shows, in line with the results of mono-substituted pyranosyl cations[32] and the results of the glucosyl cation (Figure 5), that the TS-α-$^{4}C_{1}$ pathway proceeds with more favorable orbital and electrostatic interactions, resulting from favorable HOMO–LUMO interactions (Supplementary Figure S14).[56] Increased destabilizing Pauli repulsion for the TS-α-$^{4}C_{1}$ pathway is the main contributor to the observed difference in interaction energy.[52,57] While this might seem counterintuitive, this indicates that at the same C_1•••C_{allyl} bond distance, the nucleophile is positioned more favorably in the TS-α-$^{0}S_{2}$ pathway, than in the TS-α-$^{4}C_{1}$. Inspection of the transition state structures in Figure 2, reveals that the terminal allyl methylene group is positioned under the mannose ring in the TS-α-$^{4}C_{1}$ while it approaches the cation parallel to the C=O^{+} moiety in the TS-α-$^{0}S_{2}$ avoiding steric interactions with the electrophile.

Overall, the S_E2' reactions between the mannosyl cation and weak *C*-nucleophiles (such as allyl(chloro)dimethylsilane and allyltrimethylsilane) proceed through a bottom-face (α-product-forming) addition on a boat-like $B_{2,5}$ conformation. The α-product-forming pathway that follows a $^{0}S_{2}$ trajectory is more favorable than the β-product-forming pathway passing through a chair-like transition state, as a result of significant Pauli repulsion (steric interactions) between the incoming nucleophile and the *pseudo*-axial ring substituents. The transition state resulting from a $B_{2,5}$ conformer is more favorable than the canonical α-product-forming chair-like transition state originating from the $^{4}H_{3}$-like conformation, because the former originates from a more favorable conformer while minimizing Pauli repulsion.

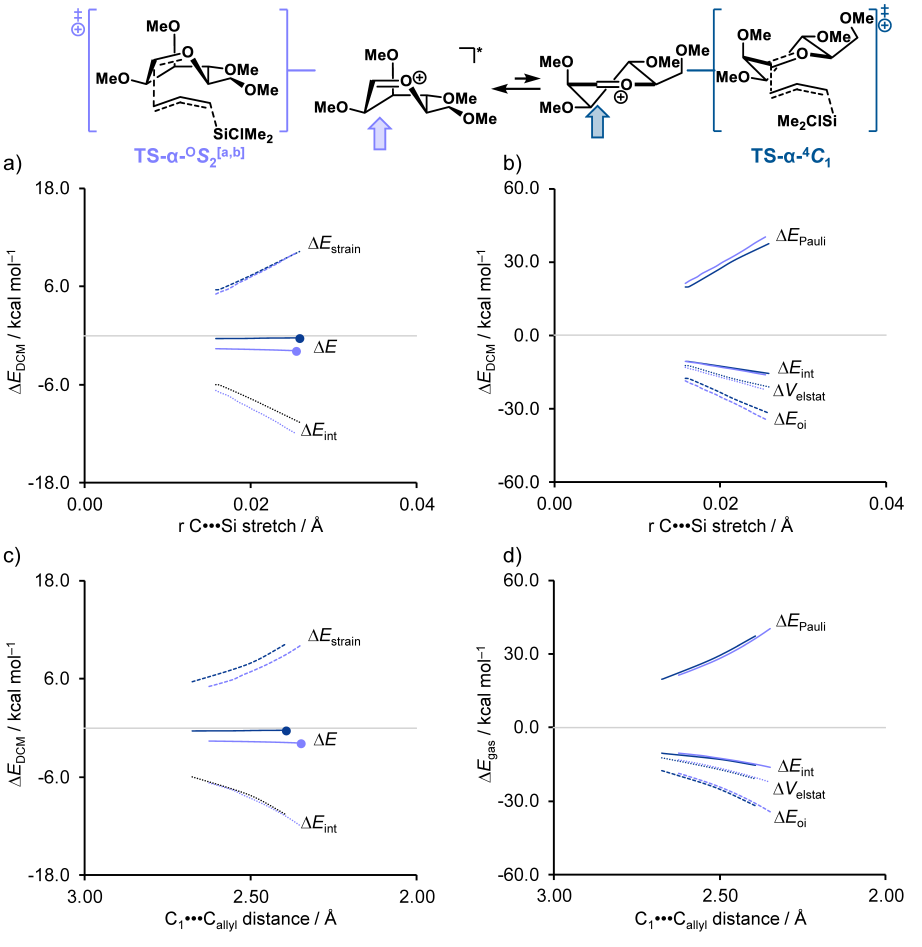

Figure 8. Activation strain (a and c) and energy decomposition analysis (b and d) for the S_E2' reactions of allyl(chloro)dimethylsilane + mannosyl cation via the α-product-forming TS-α-$^{4}C_1$ (blue) and TS-α-$^{O}S_2$ (light blue), where the energy values are plotted to the transition state (indicated by a dot), along the IRC projected on the C•••Si bond stretch (a and b) or C_1•••C_{allyl} bond distance (c and d). Energies are depicted as electronic energies and were computed at PCM(CH_2Cl_2)-B3LYP/6-311G(d,p) for ΔE_{DCM} or ZORA-B3LYP/TZ2P//PCM(CH_2Cl_2)-B3LYP/6-311G(d,p) for ΔE_{gas}. [a] The TS-α-$^{O}S_2$ pathway was plotted against the constrained potential energy surface.[41] [b] The itinerary leading up to TS-α-$^{O}S_2$ starts from a boat-like non-stationary point.

Conclusions

The stereoselectivities of *C*-glycosylation reactions critically depend on the shape and reactivity of the transiently formed glycosyl oxocarbenium ion intermediates. To accommodate the stabilization of the electron-depleted anomeric carbon atom through electron density donation by the flanking ring oxygen, oxocarbenium ions generally prefer to adopt half-chair-type structures. Addition reactions to these half chair conformers generally take place on the diastereotopic face that allows the transformation of the half chair oxocarbenium ion to the product in a chair-like conformation. This conformational scenario predicts that reactions that involve $^{3}H_{4}$-like oxocarbenium ion conformers provide the β-product, while oxocarbenium ions that favor a $^{4}H_{3}$-like structure lead to the corresponding α-product. Here it is revealed that glucosyl cations appear to adhere to this model and that the stereoselectivity of addition reactions to the glucosyl ion do not strongly depend on the nucleophilicity of the nucleophile because additions to the glucosyl cation proceed with high α-selectivity for the *C*-nucleophiles, allyl(chloro)dimethylsilane and allyltrimethylsilane, as well as the previously reported triethylsilane-*d*.[6] For the mannosyl oxocarbenium ion, a rather different picture emerges. While this ion preferentially adopts a $^{3}H_{4}$ conformation, the weak *C*-nucleophiles studied here preferentially provide the α-products, with this anomer being the solely formed product for the weakest nucleophile, allyl(chloro)dimethylsilane. This stereoselective outcome contrasts those obtained with the more reactive nucleophile triethylsilane-*d*, which provides the β-product.[6] To unravel the mechanisms responsible for the breakdown of the two-conformer model, this study has computationally investigated the possible S_N1-like reaction paths leading to the α- and β-products.

The quantum chemical computations revealed that the canonical chair-like transition states are not by definition the lowest energy barriers that can be crossed *en route* to the products. For the glucosyl oxocarbenium ion, the α-product-forming transition state in which the glucosyl ion transforms from a $^{4}H_{3}$-half chair through a $^{4}C_{1}$-like transition state was shown to be the most favorable pathway. For the reactions of the weak nucleophiles with the mannosyl ion, the higher barriers for the addition reactions allow for higher energy oxocarbenium ion conformers to become relevant reactive intermediates. Thus, while the mannosyl oxocarbenium ion has a strong preference to adopt a $^{3}H_{4}$-half chair conformation, top-face addition to this ion leads to prohibitively strong steric interactions (Pauli repulsion), especially when the transition state is later on the reaction coordinate as seen for weaker nucleophiles. These steric interactions prohibit the formation of the β-products. For the mannosyl ion, these steric interactions do not lead to an addition reaction on the other half chair ion, but rather to a favorable reaction itinerary in which the nucleophile reacts with a $B_{2,5}$-like ion to progress through a $^{O}S_{2}$-like transition state to provide the α-product. This reaction itinerary proceeds with fewer steric interactions and is reminiscent of the mechanism employed by some α-mannosidases in the hydrolysis of their substrates.[58]

Overall, the quantum chemical calculations in combination with the ASM/EDA have revealed Curtin–Hammett type kinetic scenarios for addition reactions to glycosyl cations in which the relative barrier height for the different diastereotopic addition reactions are shaped by the stabilities of the oxocarbenium ion conformers and the reactivity of the incoming nucleophiles, which dictate the timing of the transition state and the stereoelectronic interactions between the two reaction partners.

Supporting information

General Computational methods

Using density functional theory (DFT), the potential energy surfaces (PES) of glycosyl cations were calculated. The DFT computations were performed using Gaussian 09 rev D.01.[59] For all computations, the hybrid functional B3LYP[60–62] and the 6-311G(d,p)[63] basis set were used. The geometry convergence criteria were set to tight (opt=tight; max. force=$1.5 \cdot 10^{-7}$, max. displacement=$6.0 \cdot 10^{-7}$), and an internally defined super-fine grid size was used (SCF=tight, int=veryfinegrid), which is a pruned 175,974 grid for first-row atoms and a 250,974 grid for all other atoms. These parameters were chosen as recent literature indicated a significant dependence of the computed frequencies on the molecule orientation when a smaller grid size is used.[64] Geometries were optimized without symmetry constraints. All calculated stationary points have been verified by performing a vibrational analysis, to be energy minima (no imaginary frequencies) or transition states (only one imaginary frequency). The character of the normal mode associated with the imaginary frequency of the transition state has been analyzed to ensure that it is associated with the reaction of interest. If a transition state could not be located, due to instability of the associated reactant complex, a constrained potential energy surface was constructed to estimate the barrier height.[32] Solvation in CH_2Cl_2 was taken into account in the computations using the PCM solvation model. Solvent effects were explicitly used in the solving of the SCF equations and during the optimization of the geometry and the vibrational analysis. The potential energy surfaces of the studied addition reactions were obtained by performing intrinsic reaction coordinate (IRC) calculations, which, in turn, were analyzed using the PyFrag program.[65]

The denoted free Gibbs energy was calculated using Equation S1, in which $\Delta E_{\text{dichloromethane}}$ is the solution-phase energy (electronic energy), $\Delta G_{\text{dichloromethane,QH}}$ (T = 213.15 K, C = 1 M standard state) is the sum of corrections from the electronic energy to the free Gibbs energy in the quasi-harmonic oscillator approximation, including zero-point-vibrational energy. The $\Delta G_{\text{gas,QH}}$ was computed using the quasi-harmonic approximation in the solution phase according to the work of Truhlar. The quasi-harmonic approximation is the same as the harmonic oscillator approximation except for those vibrational frequencies lower than 100 cm^{-1} were raised to 100 cm^{-1} as a way to correct for the breakdown of the harmonic oscillator model for the free energies of low-frequency vibrational modes.[66,67]

$$\Delta G_{\text{dichloromethane}} = \Delta E_{\text{dichloromethane}} + \Delta G_{\text{dichloromethane,QH}} \quad \text{(S1)}$$

Solution-phase Activation Strain

The activation strain model (ASM) analysis[45–48] were performed using Gaussian 09 rev D.01.[59] The activation strain model (ASM) of chemical reactivity, also known as the distortion/interaction model, is a fragment-based approach in which the (solution-phase) reaction profiles can be described with respect to, and understood in terms of the characteristics of, the reactants. It considers the rigidity of the reactants and to which extent they need to deform during the reaction, plus their capability to interact with each other as the reaction proceeds. With the help of this model, we decompose the total energy, *i.e.,* $\Delta E_{\text{solution}}(\zeta)$, into the strain and interaction energy, $\Delta E_{\text{solution-strain}}(\zeta)$ and $\Delta E_{\text{solution-int}}(\zeta)$, respectively, and project these values onto the reaction coordinate ζ [Eq. (S2)].

$$\Delta E_{\text{solution}}(\zeta) = \Delta E_{\text{solution-strain}}(\zeta) + \Delta E_{\text{solution-int}}(\zeta) \quad \text{(S2)}$$

In this equation, the strain energy, $\Delta E_{\text{solution-strain}}(\zeta)$, is the penalty that needs to be paid to deform the reactants from their equilibrium to the geometry they adopt during the reaction at the point ζ of the reaction coordinate. On the other hand, the interaction energy, $\Delta E_{\text{solution-int}}(\zeta)$, accounts for all the chemical interactions that occur between these two deformed reactants along the reaction coordinate. The total strain energy can, in turn, be further decomposed into the strain energies corresponding to the deformation of the cation, $\Delta E_{\text{solution-strain,cation}}(\zeta)$, as well as from the nucleophile, $\Delta E_{\text{solution-strain,nucleophile}}(\zeta)$ [Eq. S3].

$$\Delta E_{\text{solution-strain}}(\zeta) = \Delta E_{\text{solution-strain,cation}}(\zeta) + \Delta E_{\text{solution-strain,allyltrimethylsilane}}(\zeta) \quad \text{(S3)}$$

In order to further analyze the interaction energy, the solution-phase potential energy surface, *i.e.,* $\Delta E_{\text{solution}}(\zeta)$, was further decomposed into the $\Delta E_{\text{solvation}}(\zeta)$, which accounts for the interaction between the solute and solvent, and the $\Delta E_{\text{solute}}(\zeta)$, which is the reaction system in gas-phase with the solution-phase geometry [Eq. S4].[68]

$$\Delta E_{\text{solution}}(\zeta) = \Delta E_{\text{solvation}}(\zeta) + \Delta E_{\text{solute}}(\zeta) \quad \text{(S4)}$$

The solute term, $\Delta E_{\text{solute}}(\zeta)$, is subsequently decomposed into the solvent-free strain, $\Delta E_{\text{solute-strain}}(\zeta)$, and interaction energy, $\Delta E_{\text{solute-int}}(\zeta)$, which are referred to as solute strain and solute interaction, respectively, to distinguish between the two solution-phase activation strain schemes [Eq. S5].

$$\Delta E_{\text{solution}}(\zeta) = \Delta E_{\text{solvation}}(\zeta) + \Delta E_{\text{solute-strain}}(\zeta) + \Delta E_{\text{solute-int}}(\zeta) \quad \text{(S5)}$$

For clarity reasons, $\Delta E_{\text{solution}}$, $\Delta E_{\text{solution-strain}}$, $\Delta E_{\text{solution-int}}$, ΔE_{solute}, $\Delta E_{\text{solute-strain}}$, and $\Delta E_{\text{solute-int}}$ are denoted as ΔE, ΔE_{strain} and ΔE_{int} in all cases, however, one can easily deduce based on the level of theory if the ΔE_{solute} or $\Delta E_{\text{solution}}$ is decomposed.

In the herein presented activation strain and accompanied energy decomposition diagrams, the intrinsic reaction coordinate (IRC) is projected onto the carbon–leaving group (C•••Si) stretch. This critical reaction coordinate undergoes a well-defined change during the reaction from the reactant complex via the transition state to the product and is shown to be a valid reaction coordinate for studying bimolecular reactions. The ASM has been used to analyze the factors affecting the reaction paths of cycloaddition reactions, nucleophilic substitution reactions, eliminations reactions as well as epoxide opening reactions.[69–73]

Energy Decomposition Analysis

The energy decomposition analysis (EDA)[74] was performed using the Amsterdam Density Functional (ADF2018.105)[75–77] software package based on the solution-phase structures obtained by Gaussian 09 rev D.01. For all computations, the B3LYP functional was used. The basis set used, denoted TZ2P, is of triple-ζ quality for all atoms and has been improved by two sets of polarization functions.[78] The accuracies of the fit scheme (Zlm fit) and the integration grid (Becke grid) were, for all calculations, set to VERYGOOD.[79,80] Relativistic effects were accounted for by using the zeroth-order regular approximation (ZORA).[81,82] The interaction energy, *i.e.,* $\Delta E_{\text{solute-int}}(\zeta)$, between the deformed reactants can be further analyzed in terms of quantitative Kohn-Sham molecular orbital (KS-MO) theory together with a canonical EDA. The EDA decomposes the $\Delta E_{\text{solute-int}}(\zeta)$ into the following three energy terms [Eq. (S6)]:

$$\Delta E_{\text{solute-int}}(\zeta) = \Delta V_{\text{elstat}}(\zeta) + \Delta E_{\text{Pauli}}(\zeta) + \Delta E_{\text{oi}}(\zeta) \quad \text{(S6)}$$

Herein, $\Delta V_{\text{elstat}}(\zeta)$ is the classical electrostatic interaction between the unperturbed charge distributions of the (deformed) reactants and is usually attractive. The Pauli repulsion, ΔE_{Pauli} (ζ), includes the destabilizing interaction between the fully occupied orbitals of both fragments due to the Pauli principle. The orbital interaction energy, $\Delta E_{\text{oi}}(\zeta)$, accounts for, amongst others, charge transfer between the fragments, such as HOMO–LUMO interactions.

Analyzing the TS-α-$^{0}S_2$ reaction paths

The S_E2' reactions between allyl(chloro)dimethylsilane and the glycosyl cations could potentially proceed through a bottom-face addition to boat-like conformation, for which the associated TS-α-$^{0}S_2$ is not a clearly defined transition state due to instability of the associated reactant complex. The electronic potential energy surface was determined from a relaxed potential energy surface scan. The starting point of each scan was the α-boat-like product complex. From here, the C-1•••allyl(chloro)dimethylsilane bond was elongated in 100 steps with a fine step size of 0.025 Å, while allowing the rest of the geometry to optimize. As a representative structure for the transition state geometry, the point on the associated relaxed potential energy surface with a similar C•••Si bond stretch as the TS-α-$^{4}C_1$ was selected.

Double consistent geometries

To make the comparison in interaction energy, between trajectories towards transition states with major differences in C_1•••allyl(chloro)dimethylsilane bond distance, a series of numerical experiments were performed. To this end, double consistent geometries were generated, whereby a consistent geometry near the transition state for TS-β-$^{1}C_4$, TS-β-$^{1}S_5$, TS-β-$^{1}S_3$, TS-α-$^{0}S_2$ and TS-α-$^{4}C_1$ at a C•••Si bond distance of 1.913 Å were taken from the IRC. The C_1•••allyl(chloro)dimethylsilane bond distance was to 2.413 Å (Supplementary Figure S15). Note that these geometries are not optimized, instead, they are taken from the IRC, and key bond distances are constrained to match a selected reference structure.

Supplementary Figures

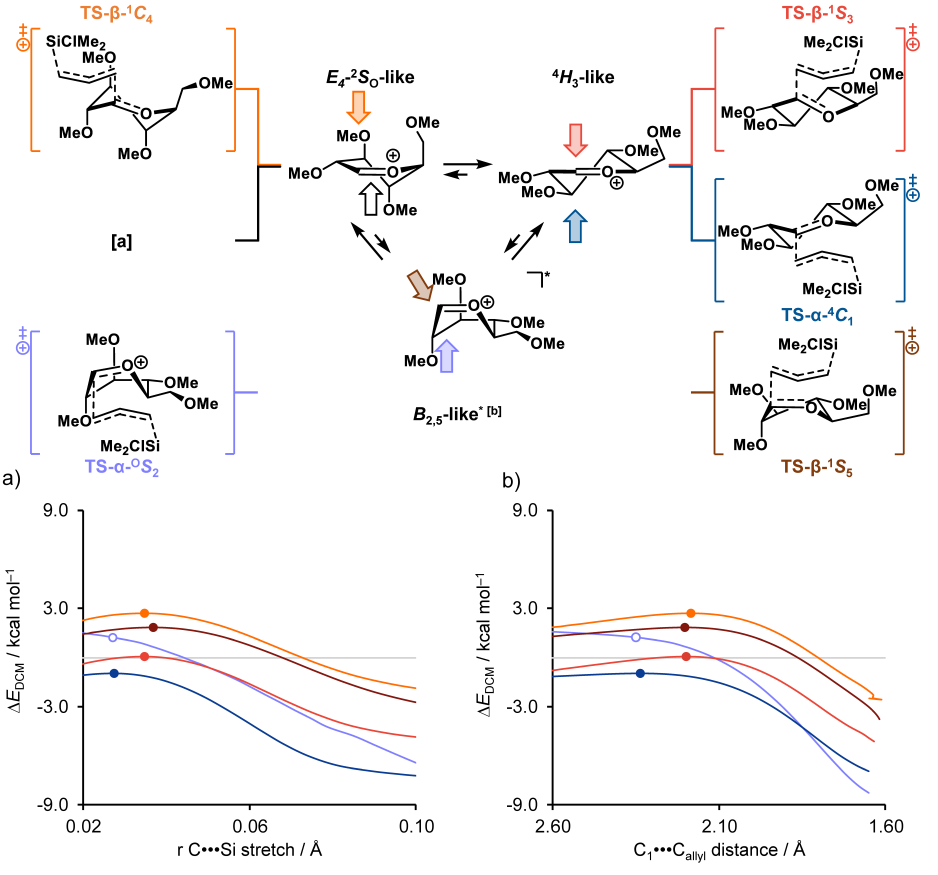

Supplementary Figure S1. The possible S_E2' reaction pathways of the addition of allyl(chloro)dimethylsilane to the glucosyl cation, via the following transition states: TS-β-$^1C_4$ (orange), TS-β-$^1S_5$ (brown), TS-β-$^1S_3$ (red), TS-α-$^OS_2$ (light blue) and TS-α-$^4C_1$ (blue). Energy values are plotted along the IRC projected on the C•••Si bond stretch (a) or C_1•••C_{allyl} bond distance (b). Transition states are indicated by a filled dot. The representative structure of the TS-α-$^OS_2$ is indicated by a non-filled dot. Energies are depicted as electronic energies and were computed at PCM(CH_2Cl_2)-B3LYP/6-311G(d,p). [a] A representative structure for the transition state geometry was used.[41] [b] The itinerary leading up to TS-α-$^OS_2$ and TS-β-$^1S_5$ start from a boat-like non-stationary point.

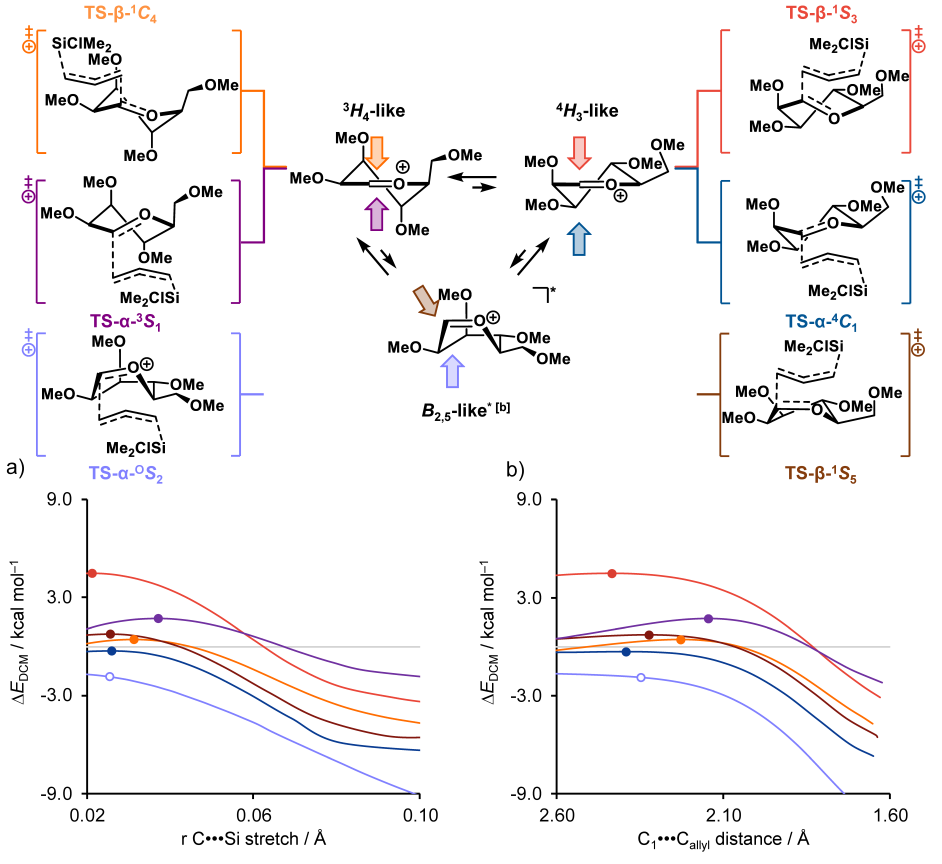

Supplementary Figure S2. The possible S_E2' reaction pathways of the addition of allyl(chloro)dimethylsilane to the mannosyl cation, via the following transition states: TS-β-$^{1}C_4$ (orange), TS-β-$^{1}S_5$ (brown), TS-β-$^{1}S_3$ (red), TS-α-$^{O}S_2$ (light blue) and TS-α-$^{4}C_1$ (blue). Energy values are plotted along the IRC projected on the C•••Si bond stretch (a) or C_1•••C_{allyl} bond distance (b). Transition states are indicated by a filled dot. The representative structure of the TS-α-$^{O}S_2$ is indicated by a non-filled dot. Energies are depicted as electronic energies and were computed at PCM(CH_2Cl_2)-B3LYP/6-311G(d,p). [a] A representative structure for the transition state geometry was used.[41] [b] The itinerary leading up to TS-α-$^{O}S_2$ and TS-β-$^{1}S_5$ start from a boat-like non-stationary point.

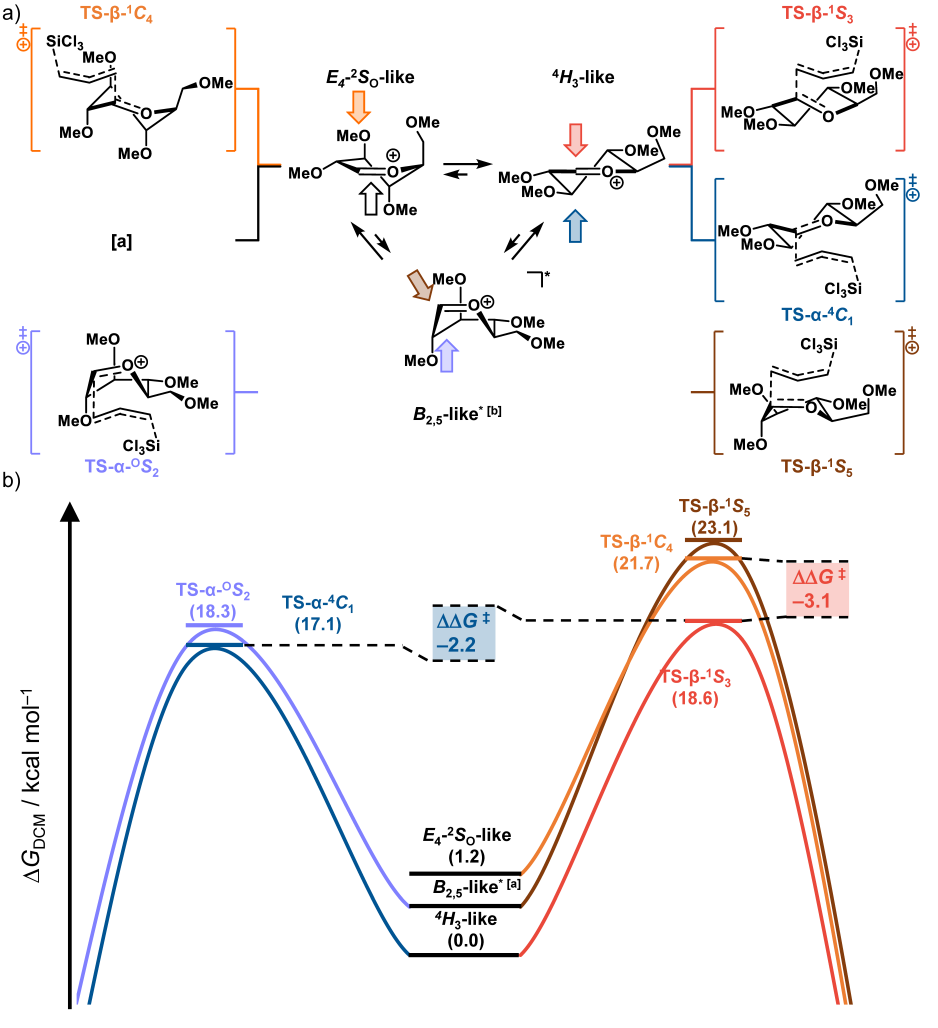

Supplementary Figure S3. The possible S_E2' reaction pathways (a) and the corresponding reaction profile (b) of the addition of allyltrichlorosilane to the glucosyl cation, via the following transition states: TS-β-$^{1}C_4$ (orange), TS-β-$^{1}S_5$ (brown), TS-β-$^{1}S_3$ (red), TS-α-$^{O}S_2$ (light blue) and TS-α-$^{4}C_1$ (blue). Energies are depicted as Gibbs free energies (T = 213.15 K) and were computed at PCM(CH_2Cl_2)-B3LYP/6-311G(d,p). [a] The itinerary leading up to TS-α-$^{O}S_2$ and TS-β-$^{1}S_5$ start from a boat-like non-stationary point.

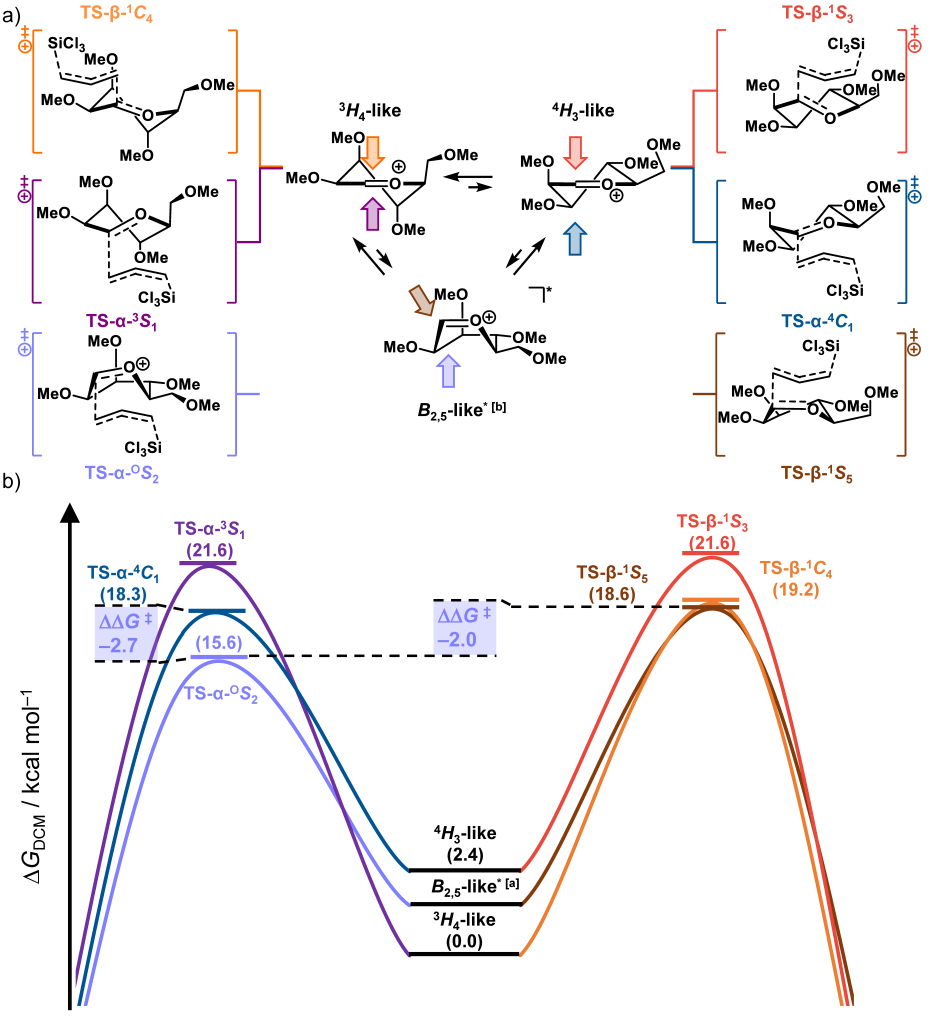

Supplementary Figure S4. The possible S_E2' reaction pathways (a) and the corresponding reaction profile (b) of the addition of allyltrichlorosilane to the mannosyl cation, via the following transition states: TS-β-$^1C_4$ (orange), TS-β-$^1S_5$ (brown), TS-β-$^1S_3$ (red), TS-α-$^OS_2$ (light blue), TS-α-$^3S_1$ (purple), and TS-α-$^4C_1$ (blue). Energies are depicted as Gibbs free energies (T = 213.15 K) and were computed at PCM(CH_2Cl_2)-B3LYP/6-311G(d,p). [a] The itinerary leading up to TS-α-$^OS_2$ and TS-β-$^1S_5$ start from a boat-like non-stationary point.

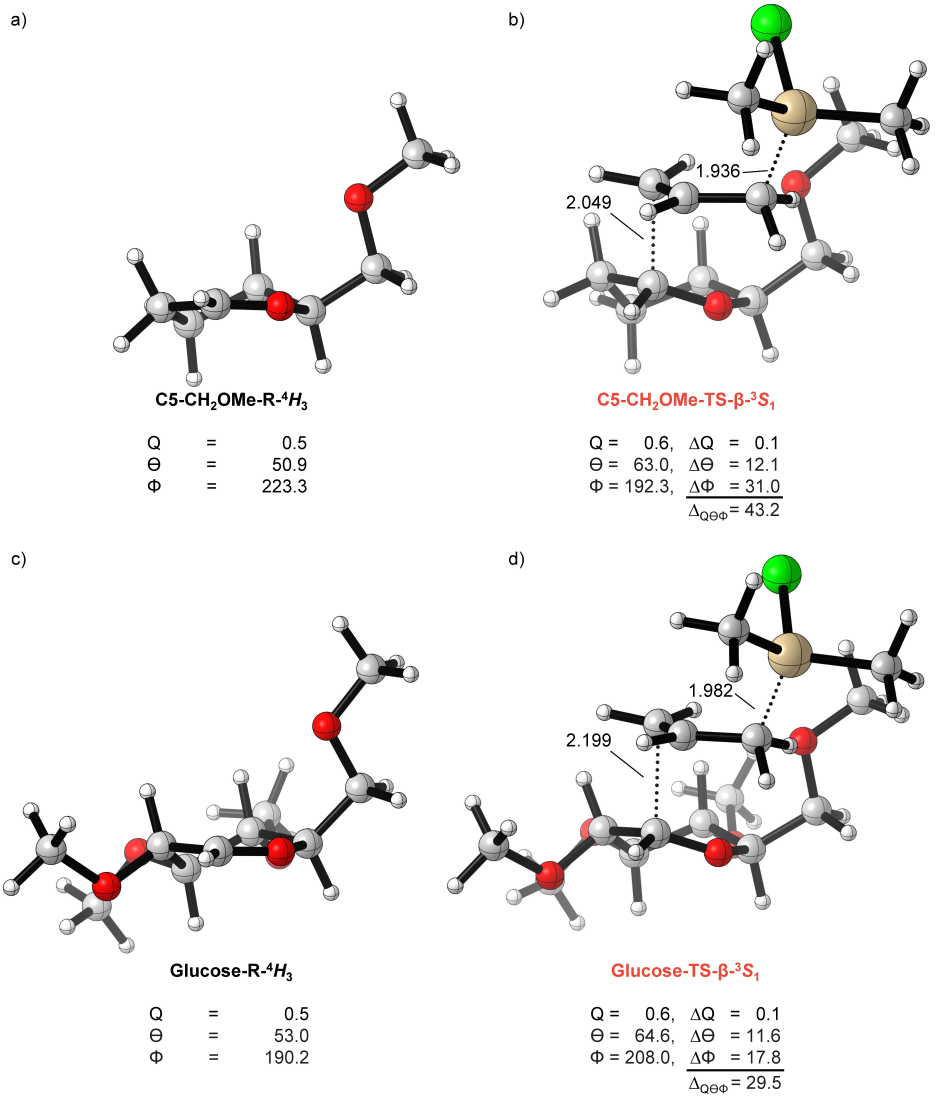

Supplementary Figure S5. Mono-substituted C5-CH_2OMe (a and b) and glucose (c and d) pyranosyl cation structures[42] of the $^4H_3$ conformation (a and c), and the TS-β-$^1S_3$ transition state (b and d) geometries. Key distances are given in Å. The Cremer Pople puckering parameters (Q, Θ and Φ), defining the conformation of the glycosyl cation, are given below each structure. Below each transition state geometry the difference between the Cremer Pople puckering parameters of the transition state and the reactant are given (ΔQ, ΔΘ and ΔΦ), as well as their sum ($\Delta_{Q\Theta\Phi}$)

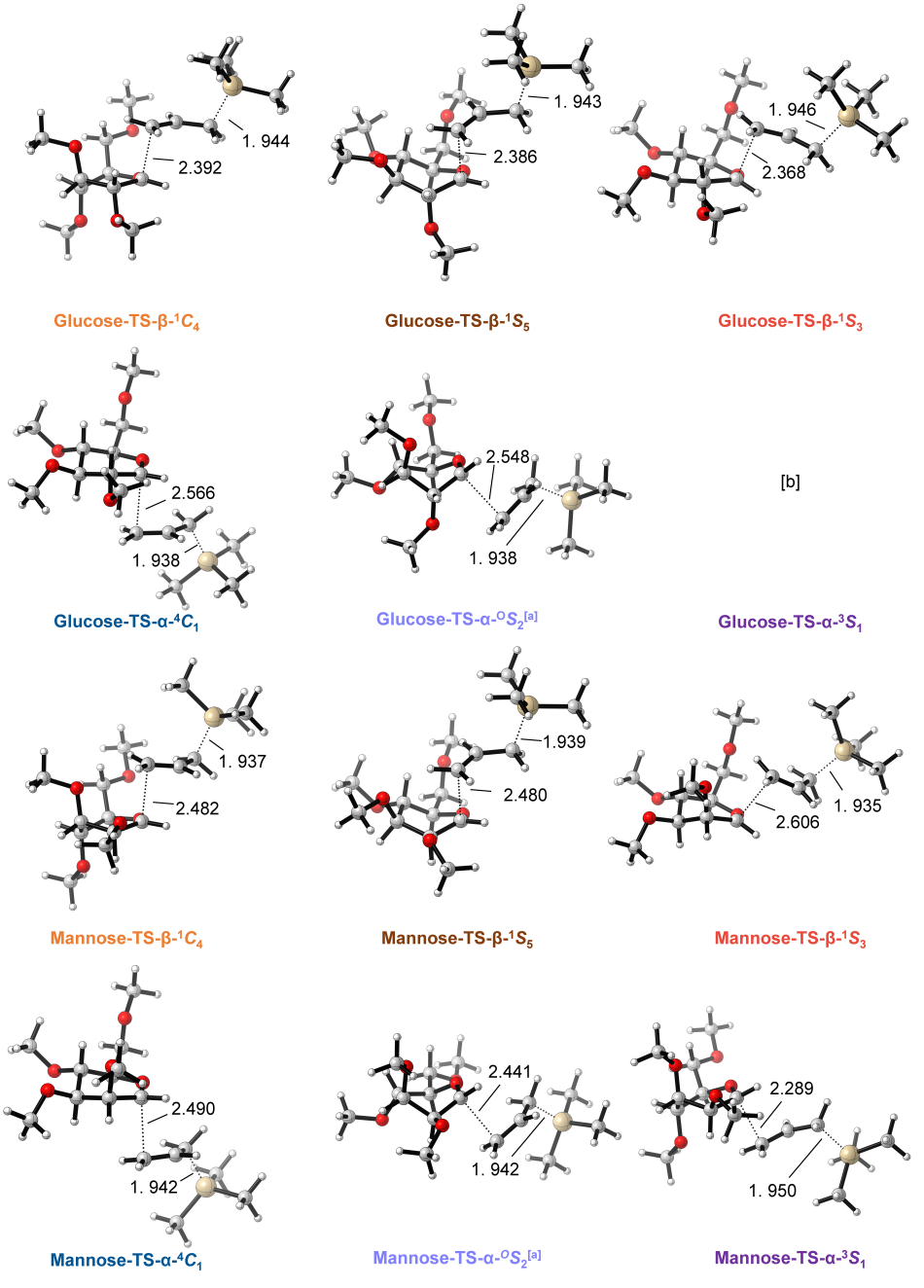

Supplementary Figure S6. Structures[42] of the transition state geometries of the S_E2' reactions between allyltrimethylsilane and the glucosyl or mannosyl cations. Key distances are given in Å. [a] A representative structure for the transition state geometry was used.[41] [b] The bottom-side attack on the $^{3}H_{4}$ yields is unfavorable, instead the glycosyl cations deform to other transition state shapes during searches.

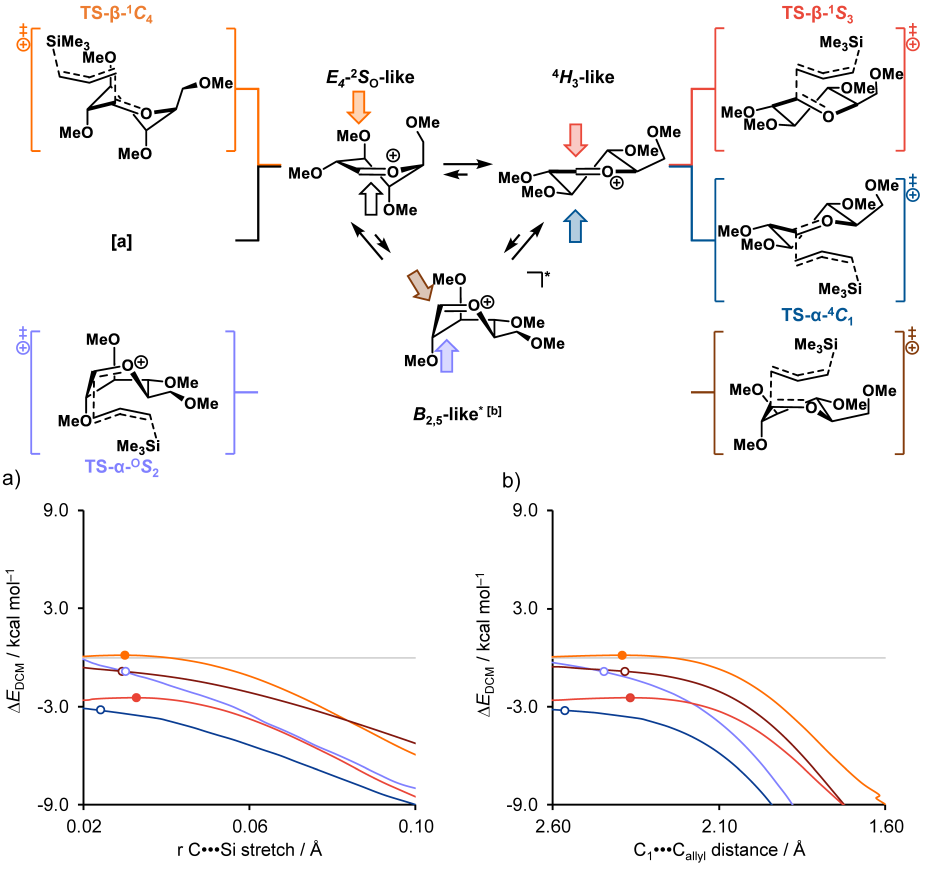

Supplementary Figure S7. The possible S_E2' potential energy surfaces of the addition of allyltrimethylsilane to the glucosyl cation, via the following transition states: TS-β-$^1C_4$ (orange), TS-β-$^1S_5$ (brown), TS-β-$^1S_3$ (red), TS-α-$^OS_2$ (light blue) and TS-α-$^4C_1$ (blue). Energy values are plotted along the IRC projected on the C•••Si bond stretch (a) or C_1•••C_{allyl} bond distance (b). Transition states are indicated by a filled dot. The representative structure of the TS-α-$^OS_2$, TS-α-$^4C_1$ and TS-β-$^1S_5$ are indicated by a non-filled dot. Energies are depicted as electronic energies and were computed at PCM(CH_2Cl_2)-B3LYP/6-311G(d,p). [a] A representative structure for the transition state geometry was used.[41] [b] As a transition state, the local maximum on the Gibbs free potential energy surface was used. [c] The itinerary leading up to TS-α-$^OS_2$ and TS-β-$^1S_5$ start from a boat-like non-stationary point.

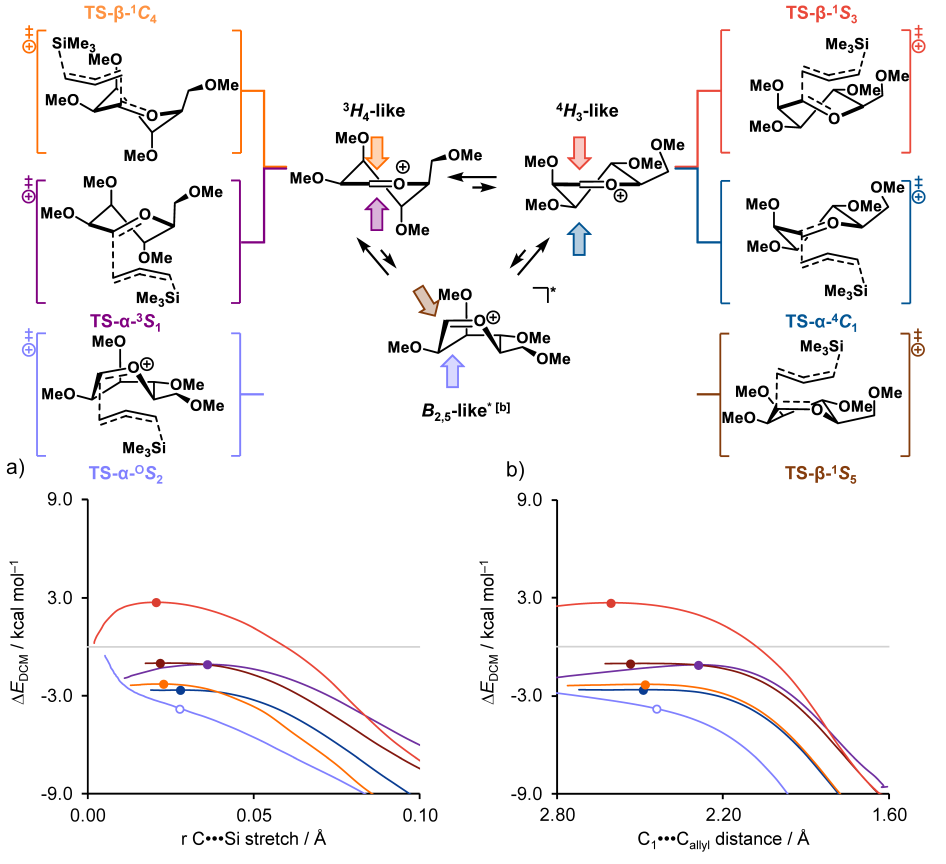

Supplementary Figure S8. The possible S_E2' potential energy surfaces of the addition of allyltrimethylsilane to the mannosyl cation, via the following transition states: TS-β-$^1C_4$ (orange), TS-β-$^1S_5$ (brown), TS-β-$^1S_3$ (red), TS-α-$^0S_2$ (light blue) and TS-α-$^4C_1$ (blue). Energy values are plotted along the IRC projected on the C•••Si bond stretch (a) or C_1•••C_{allyl} bond distance (b). Transition states are indicated by a filled dot. The representative structure of the TS-α-$^0S_2$ is indicated by a non-filled dot. Energies are depicted as electronic energies and were computed at PCM(CH_2Cl_2)-B3LYP/6-311G(d,p). [a] A representative structure for the transition state geometry was used.[41] [b] The itinerary leading up to TS-α-$^0S_2$ and TS-β-$^1S_5$ start from a boat-like non-stationary point.

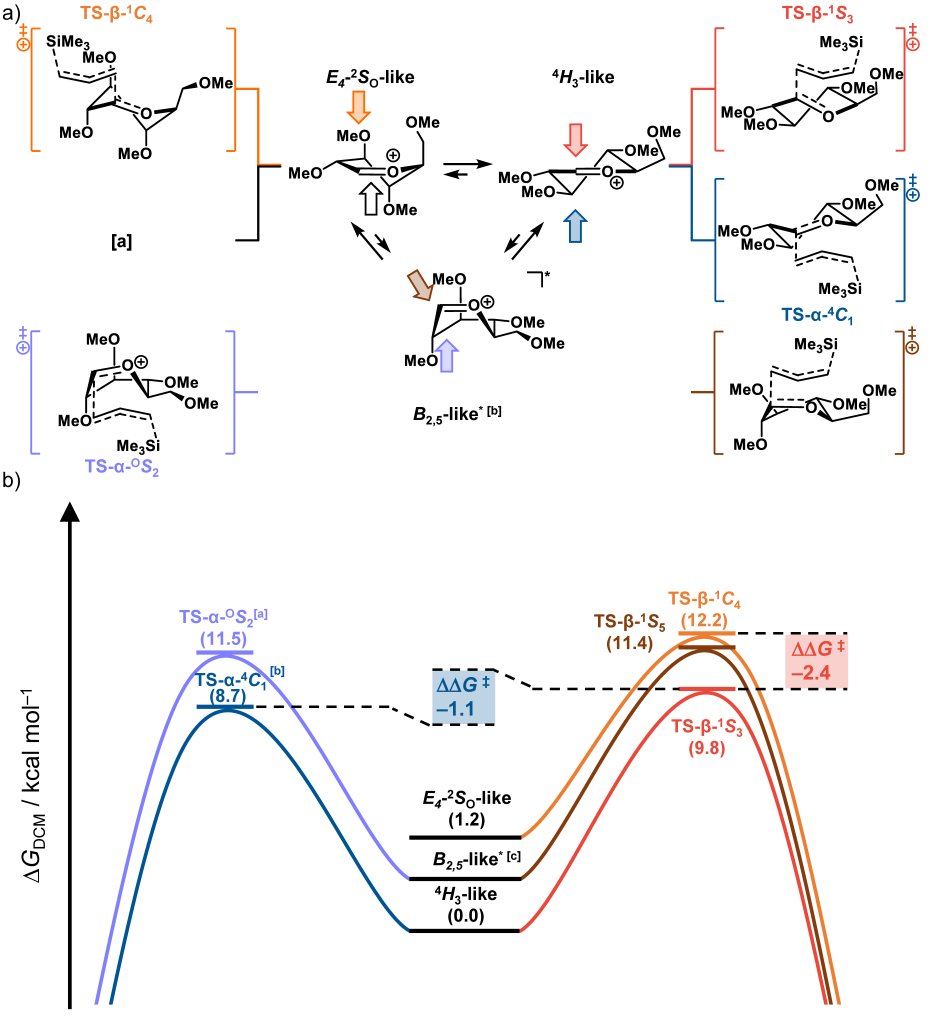

Supplementary Figure S9. The possible S_E2' reaction pathways (a) and the corresponding reaction profile (b) of the addition of allyltrimethylsilane to the glucosyl cation, via the following transition states: TS-β-$^1C_4$ (orange), TS-β-$^1S_5$ (brown), TS-β-$^1S_3$ (red), TS-α-$^OS_2$ (light blue) and TS-α-$^4C_1$ (blue). Energies are depicted as Gibbs free energies (T = 213.15 K) and were computed at PCM(CH_2Cl_2)-B3LYP/6-311G(d,p). [a] A representative structure for the transition state geometry was used.[41] [b] As a transition state, the local maximum on the Gibbs free potential energy surface was used. [c] The itinerary leading up to TS-α-$^OS_2$ and TS-β-$^1S_5$ start from a boat-like non-stationary point.

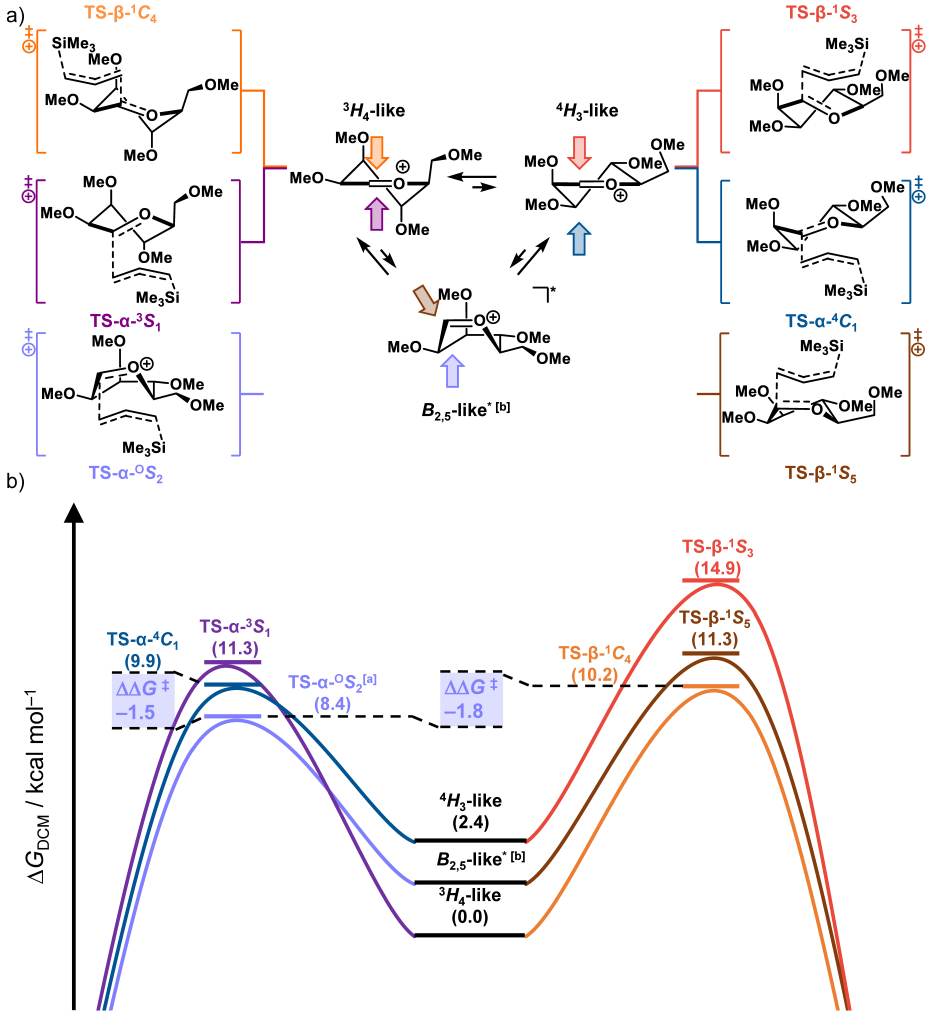

Supplementary Figure S10. The possible S_E2' reaction pathways (a) and the corresponding reaction profile (b) of the addition of allyltrimethylsilane to the mannosyl cation, via the following transition states: TS-β-$^1C_4$ (orange), TS-β-$^1S_5$ (brown), TS-β-$^1S_3$ (red), TS-α-$^OS_2$ (light blue), TS-α-$^3S_1$ (purple), and TS-α-$^4C_1$ (blue). Energies are depicted as Gibbs free energies (T = 213.15 K) and were computed at PCM(CH_2Cl_2)-B3LYP/6-311G(d,p). [a] A representative structure for the transition state geometry was used.[41] [b] The itinerary leading up to TS-α-$^OS_2$ and TS-β-$^1S_5$ start from a boat-like non-stationary point.

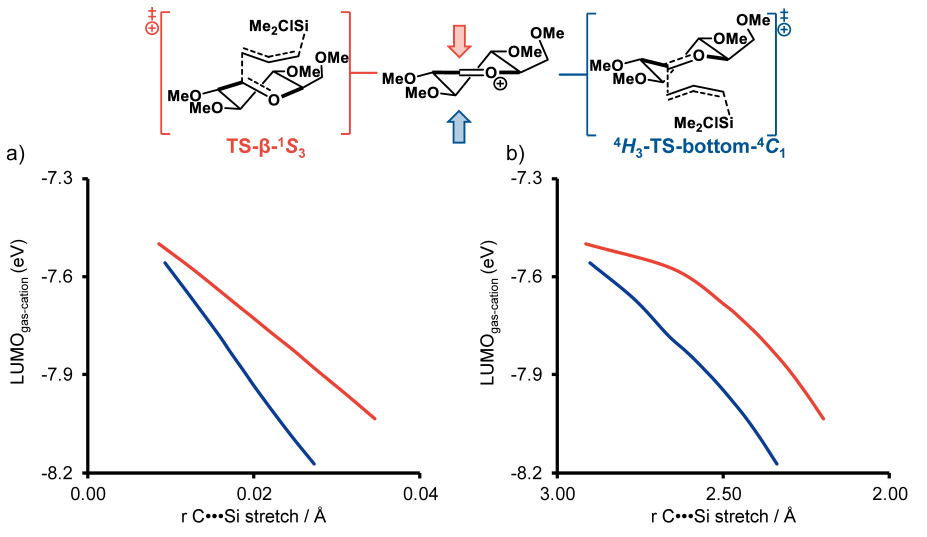

Supplementary Figure S11. (a) The LUMO energy (in eV) of the glucosyl cation during the S_E2' reactions of allyl(chloro)dimethylsilane + glucosyl cation via the α-product forming TS-α-$^4C_1$ (blue) and via the β-product forming TS-β-$^1S_3$ (red), along the IRC projected on the C•••Si bond stretch (a) or the C_1•••C_{allyl} bond distance (b). Energies are depicted as electronic energies and were computed at ZORA-B3LYP/TZ2P//PCM(CH_2Cl_2)-B3LYP/6-311G(d,p).

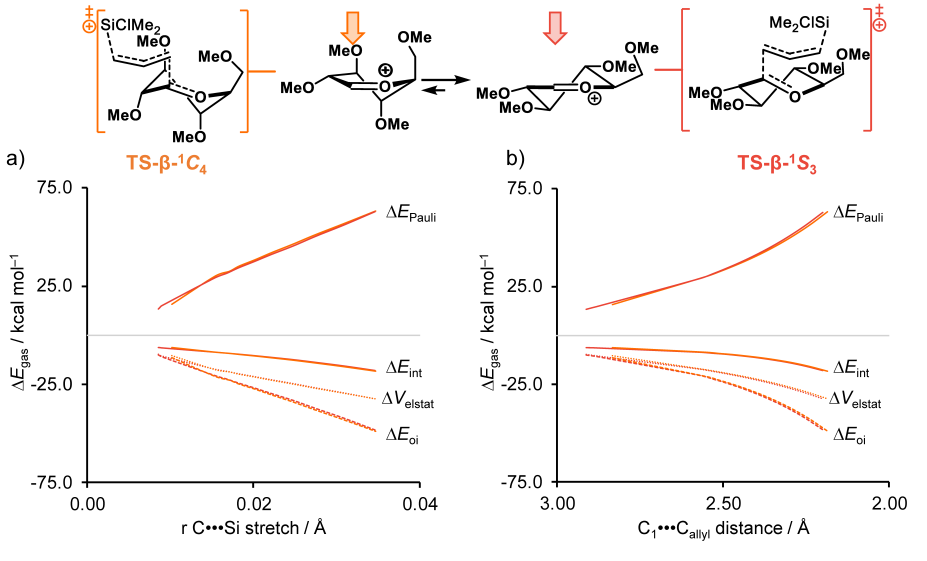

Supplementary Figure S12. Energy decomposition analysis for the S_E2' reactions of allyl(chloro)dimethylsilane + glucosyl cation via the β-product forming TS-β-$^1C_4$ (orange) and via the β-product forming TS-β-$^1S_3$ (red), where the energy values are plotted to the transition state (indicated by a dot), along the IRC projected on the C•••Si bond stretch (a) or C_1•••C_{allyl} bond distance (b). Energies are depicted as electronic energies and were computed at ZORA-B3LYP/TZ2P//PCM(CH_2Cl_2)-B3LYP/6-311G(d,p).

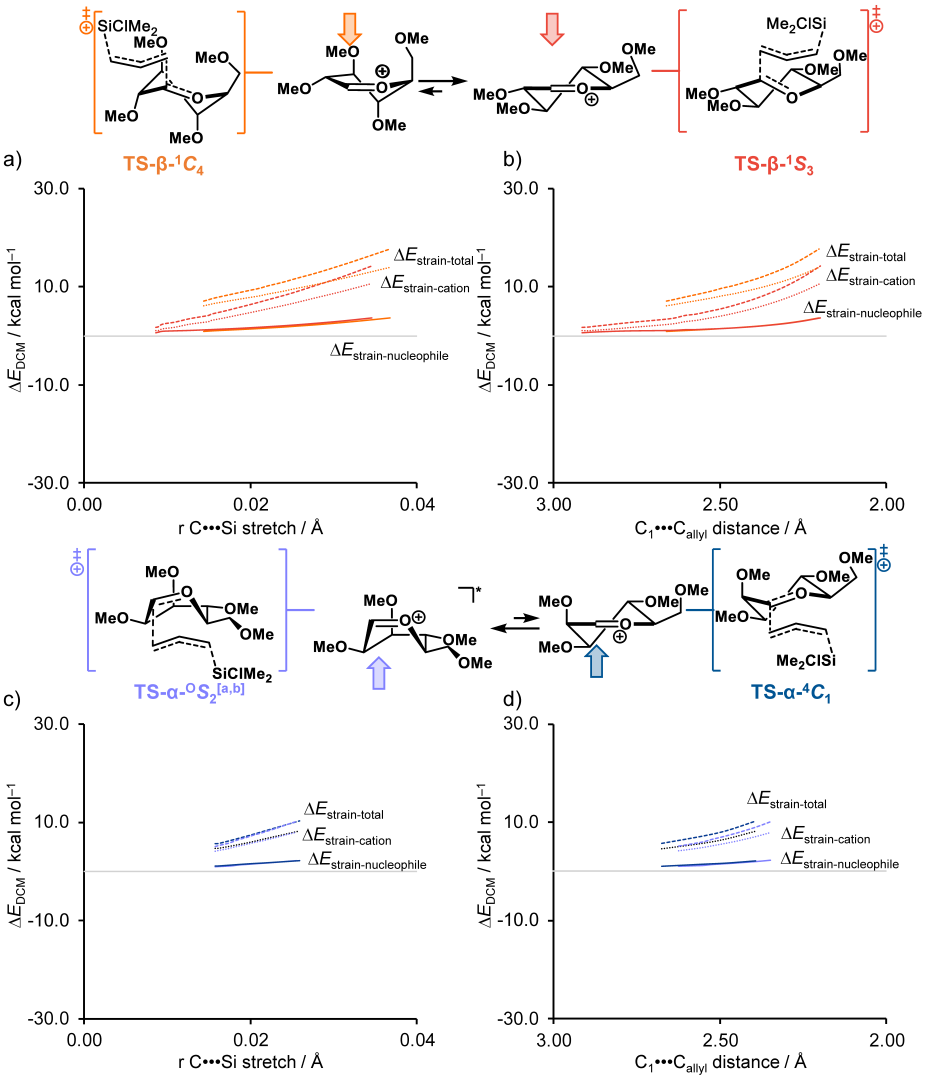

Supplementary Figure S13. Activation strain analysis , showing only the decomposed strain term, for the S_E2' reactions of allyl(chloro)dimethylsilane + glucosyl cation via the α-product forming TS-β-$^1C_4$ (orange) and the TS-β-$^1S_3$ (red), along the IRC projected on the C•••Si bond stretch (a) and C_1•••C_{allyl} distance (b). Activation strain analysis , showing only the decomposed strain term, for the S_E2' reactions of allyl(chloro)dimethylsilane + mannosyl cation via the α-product forming TS-α-$^OS_2$ (light blue) and the TS-α-$^4C_1$ (blue), along the IRC projected on the C•••Si bond stretch (c) and C_1•••C_{allyl} bond distance (d). Energies are depicted as electronic energies and were computed at PCM(CH_2Cl_2)-B3LYP/6-311G(d,p). [a] The TS-α-$^OS_2$ pathway was plotted against the constrained potential energy surface.[41] [b] The itinerary leading up to TS-α-$^OS_2$ starts from a boat-like non-stationary point.

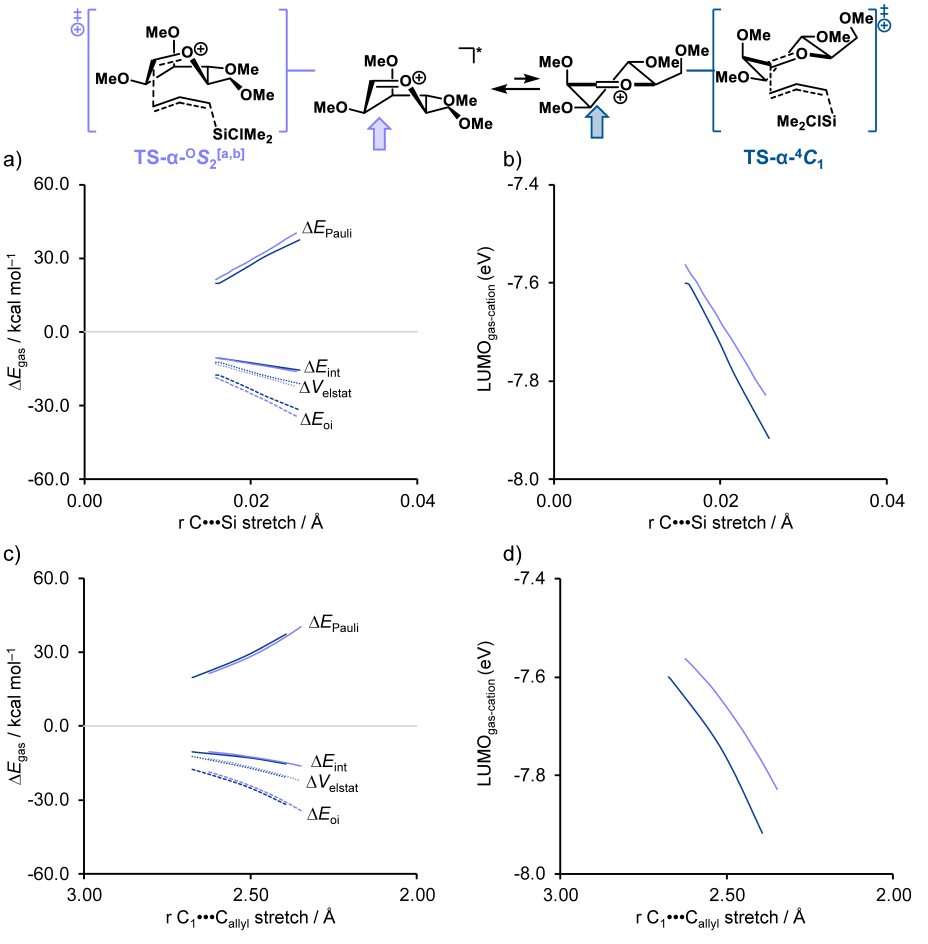

Supplementary Figure S14. Energy decomposition analysis (a and c) and LUMO energy (in eV) of the mannosyl cation (b and d) for the S_E2' reactions of allyl(chloro)dimethylsilane + mannosyl cation via the α-product forming TS-α-$^{4}C_1$ (blue) and via the α-product forming TS-α-$^{O}S_2$ (light blue), along the IRC projected on the C•••Si bond stretch (a and b) and the C_1•••C_{allyl} bond distance (c and d). Energies are depicted as electronic energies and were computed at ZORA-B3LYP/TZ2P//PCM(CH_2Cl_2)-B3LYP/6-311G(d,p). [b] The itinerary leading up to TS-α-$^{O}S_2$ starts from a boat-like non-stationary point.

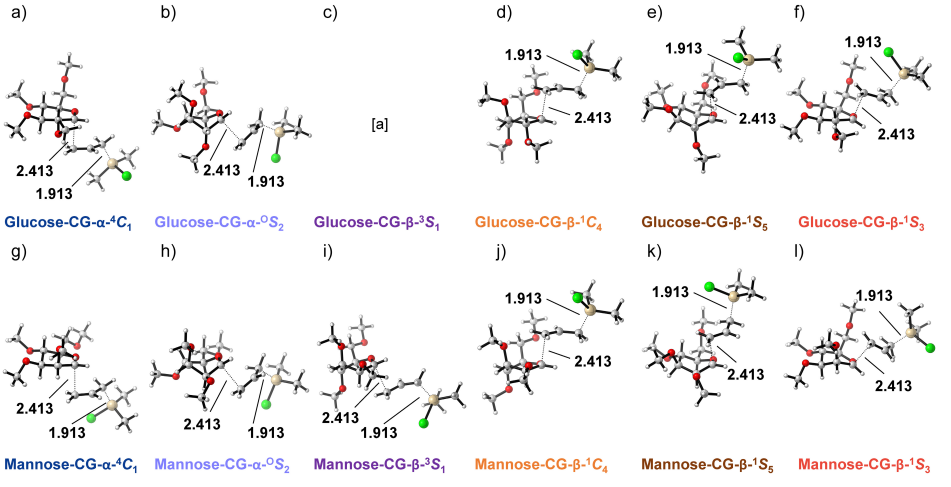

m)

Glucosyl	ΔE_{DCM}	$\Delta E_{DCM\text{-}strain\text{-}total}$	$\Delta E_{DCM\text{-}strain\text{-}cation}$	$\Delta E_{DCM\text{-}strain\text{-}nucleophile}$	$\Delta E_{DCM\text{-}int}$	$\Delta E_{gas\text{-}int}$	$\Delta E_{gas\text{-}Pauli}$	$\Delta E_{gas\text{-}oi}$	$\Delta V_{gas\text{-}elstat}$
CG-α-$^4C_1$	–0.7	+6.9	+5.9	+1.0	–7.6	–11.6	+41.4	–31.1	–21.9
CG-α-$^OS_2$	+1.6	+10.1	+9.0	+1.1	–8.5	–12.0	+37.8	–29.7	–20.1
CG-β-$^1C_4$	+2.4	+9.5	+7.8	+1.7	–7.1	–10.6	+39.9	–28.4	–22.1
CG-β-$^1S_5$	+1.9	+9.2	+7.7	+1.4	–7.3	–11.4	+41.6	–30.1	–22.9
CG-β-$^1S_3$	–0.2	+6.5	+4.8	+1.7	–6.7	–10.3	+40.9	–28.7	–22.5
Mannosyl	ΔE_{DCM}	$\Delta E_{DCM\text{-}strain\text{-}total}$	$\Delta E_{DCM\text{-}strain\text{-}cation}$	$\Delta E_{DCM\text{-}strain\text{-}nucleophile}$	$\Delta E_{DCM\text{-}int}$	$\Delta E_{gas\text{-}int}$	$\Delta E_{gas\text{-}Pauli}$	$\Delta E_{gas\text{-}oi}$	$\Delta V_{gas\text{-}elstat}$
CG-α-$^4C_1$	–0.2	+7.0	+5.6	+1.4	–6.8	–11.7	+38.5	–29.3	–20.9
CG-α-$^OS_2$	–1.7	+7.3	+5.8	+1.5	–9.0	–13.1	+35.6	–28.9	–19.8
CG-α-$^3S_1$	1.1	+6.6	+4.9	+1.7	–5.5	–9.6	+36.5	–26.1	–20.0
CG-β-$^1C_4$	+0.2	+8.4	+6.8	+1.6	–8.2	–11.8	+39.6	–29.2	–22.2
CG-β-$^1S_5$	+0.7	+10.7	+9.1	+1.6	–10.0	–13.8	+40.1	–31.6	–22.3
CG-β-$^1S_3$	+4.8	+12.2	+11.3	+0.9	–7.4	–10.1	+41.5	–30.5	–21.1

Supplementary Figure S15. Illustrations[42] of double consistent (C•••Si and C_1•••C_{allyl} bond distance) geometries of S_E2' reactions of allyl(chloro)dimethylsilane + glucosyl cations via TS-α-$^4C_1$ (a), TS-α-$^OS_2$ (b), TS-α-$^3S_1$ (c), TS-β-$^1C_4$ (d), TS-β-$^1S_5$ (e) and TS-β-$^1S_3$ (f) pathways, and mannosyl cation via TS-α-$^4C_1$ (g), TS-α-$^OS_2$ (h), TS-α-$^3S_1$ (i), TS-β-$^1C_4$ (j), TS-β-$^1S_5$ (k) and TS-β-$^1S_3$ (l) pathways. Key distances are given in Å. Energies at this geometry are given (m) and were computed at PCM(CH_2Cl_2)-B3LYP/6-311G(d,p) (ΔE_{DCM}) and for the EDA analysis at ZORA-B3LYP/TZ2P//PCM(CH_2Cl_2)-B3LYP/6-311G(d,p) (ΔE_{gas}). [a] The bottom-side attack on the $^3H_4$ yields is unfavorable, instead the glycosyl cations deform to other transition state shapes during searches.

Supplementary Table S1. PCM(CH_2Cl_2)-B3LYP/6-311G(d,p) Gibbs energies (ΔG_{DCM}, in kcal mol^{-1}) and in parentheses electronic energies (ΔE_{DCM}, in kcal mol^{-1}) in CH_2Cl_2 relative to reactants of the stationary points of the S_E2' reaction between allyltrichlorosilane ($CH_2CHCH_2SiCl_3$), allyl(chloro)dimethylsilane ($CH_2CHCH_2SiClMe_2$) or allyltrimethylsilane ($CH_2CHCH_2SiMe_3$) and the glucosyl or mannosyl oxocarbenium ions. All energies (R, TS, and P) are reported relative to the lowest energy conformer.

	Glucosyl Cation +					
	$CH_2CHCH_2SiCl_3$		**$CH_2CHCH_2SiClMe_2$**		**$CH_2CHCH_2SiMe_3$**	
TS-α-$^{0}S_2$	18.3	(5.4)	13.5	(1.0)	11.5	(−0.7)
TS-α-$^{4}C_1$	17.1	(3.9)	11.2	(−1.2)	8.7	(−3.5)
TS-α-$^{3}S_1$	[a]		[a]		[a]	
TS-β-$^{1}C_4$	21.7	(8.3)	15.3	(2.5)	12.2	(−0.1)
TS-β-$^{1}S_5$	21.3	(8.1)	14.3	(1.6)	11.4	(−1.1)
TS-β-$^{1}S_3$	18.5	(5.5)	12.8	(−0.2)	9.8	(−2.7)
P-α	−26.2	(−39.0)	−38.6	(−51.7)	−45.0	(−58.1)
P-β	−28.9	(−41.4)	−41.3	(−54.1)	−47.7	(−60.6)
	Mannosyl Cation +					
	$CH_2CHCH_2SiCl_3$		**$CH_2CHCH_2SiClMe_2$**		**$CH_2CHCH_2SiMe_3$**	
TS-α-$^{0}S_2$	15.6	(2.6)	10.8	(−1.9)	8.4	(−3.8)
TS-α-$^{4}C_1$	18.3	(4.9)	12.5	(−0.3)	9.9	(−2.6)
TS-α-$^{3}S_1$	21.6	(7.9)	14.6	(1.7)	11.3	(−1.1)
TS-β-$^{1}C_4$	19.2	(5.9)	13.0	(0.4)	10.2	(−2.3)
TS-β-$^{1}S_5$	18.6	(5.2)	13.4	(0.7)	11.3	(−1.0)
TS-β-$^{1}S_3$	21.6	(8.5)	17.2	(4.5)	14.9	(2.7)
P-α	−24.4	(−37.3)	−36.8	(−50.0)	−43.2	(−56.5)
P-β	−27.3	(−40.1)	−39.7	(−52.8)	−46.2	(−59.2)

General experimental procedures
All chemicals (Acros, Fluka, Merck, and Sigma-Aldrich) were used as received unless stated otherwise. Dichloromethane was stored over activated 4 Å molecular sieves (beads, 8-12 mesh, Sigma-Aldrich). Before use traces of water present in the donor, diphenyl sulfoxide (Ph_2SO) and tri-*tert*-butylpyrimidine (TTBP) were removed by co-evaporation with dry toluene. The acceptors were stored in stock solutions (DCM, 0.5 M) over activated 3 Å molecular sieves (rods, size 1/16 in., Sigma-Aldrich). Trifluoromethanesulfonic anhydride (Tf_2O) was distilled over P_2O_5 and stored at −20 °C under a nitrogen atmosphere. Overnight temperature control was achieved by an FT902 Immersion Cooler (Julabo). Column chromatography was performed on silica gel 60 Å (0.04 – 0.063 mm, Screening Devices B.V.). TLC-analysis was conducted on TLC Silica gel 60 (Kieselgel 60 F_{254}, Merck) with UV detection by (254 nm) and by spraying with 20% sulfuric acid in ethanol followed by charring at ± 150 °C or by spraying with a solution of $(NH_4)_6Mo_7O_{24}{\cdot}H_2O$ (25 g/l) and $(NH_4)_4Ce(SO_4)4{\cdot}_2H_2O$ (10 g/l) in 10% sulfuric acid in water followed by charring at ± 250 °C. High-resolution mass spectra were recorded on a Thermo Finnigan LTQ Orbitrap mass spectrometer equipped with an electrospray ion source in positive mode (source voltage 3.5 kV, sheath gas flow 10, capillary temperature 275 °C) with resolution R=60.000 at m/z=400 (mass range = 150-4000). ^{1}H and ^{13}C NMR spectra were recorded on a Bruker AV-400 NMR instrument (400 and 101 MHz respectively), a Bruker AV-500 NMR instrument (500 and 126 MHz respectively), or a Bruker AV-600 NMR instrument (600 and 151 MHz respectively). For samples measured in $CDCl_3$ chemical shifts (δ) are given in ppm relative to tetramethylsilane as an internal standard or the residual signal of the deuterated solvent. Coupling constants (*J*) are given in Hz. To get better resolution of signals with small coupling constants or overlapping signals a gaussian window function (LB ± -1 and GB ± 0.5) was used on the ^{1}H NMR spectrum. All given ^{13}C APT spectra are proton decoupled. NMR peak assignment was made using COSY, HSQC. If necessary additional NOESY, HMBC and HMBC-GATED experiments were used to elucidate the structure further. The anomeric product ratios were based on the integration of ^{1}H.

General glycosylation procedure: pre-activation Tf_2O/Ph_2SO based *C*-glycosylation.
A solution of the donor (100 µmol), Ph_2SO (26 mg, 130 µmol, 1.3 equiv) and TTBP (62 mg, 250 µmol, 2.5 equiv) in DCM (2 mL, 0.05 M) was stirred over activated 3 Å molecular sieves (rods, size 1/16 in., Sigma-Aldrich) for 30 min under an atmosphere of N_2. The solution was cooled to −80 °C and Tf_2O (22 µl, 130 µmol, 1.3 equiv) was slowly added to the reaction mixture. The reaction mixture was allowed to warm to −60 °C in approximately 45 min, followed by cooling to −80 °C and the addition of the acceptor (200 µmol, 2 equiv) in DCM (0.4 mL, 0.5 M). The reaction was allowed to warm up to −60 °C and stirred for an additional 18 h at this temperature until full reaction completion was observed. The reaction was quenched with sat. aq. $NaHCO_3$ at −60 °C and diluted with DCM (5 mL). The resulting solution was washed with H_2O and brine, dried over $MgSO_4$, filtered and concentrated under reduced pressure. Purification by column chromatography yielded the corresponding *C*-coupled glycoside. The anomeric ratio of both the crude product and the purified product were determined from ^{1}H-NMR, and subsequently compared to ensure no alteration of the anomeric ratio as a result of column chromatography.

Synthetic procedures of glycosylation products

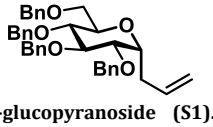

1-allyl-1-deoxy-2,3,4,6-tetra-*O*-benzyl-D-glucopyranoside (S1). The title compound was prepared according to the general glycosylation procedure, using glucose donor **1**[6] and allyl(chloro)dimethylsilane (0.058 mmol, 33 mg, 58%, >98:2, α:β) or allyltrimethylsilane (0.048 mmol, 27 mg, 48%, >98:2, α:β), yielding the title compound as a colorless oil. ^{1}H NMR (400 MHz, $CDCl_3$, HH-COSY, HSQC, HMBC, HMBC-GATED) δ 7.36 – 7.24 (m, 20H, CH_{Arom}), 5.81 (ddt, *J* = 17.2, 10.2, 6.8 Hz, 1H, CH_2-C*H*=CH_2), 5.14 – 5.03 (m, 2H, CH_2-CH=CH_2), 4.93 (d, *J* = 10.9 Hz, 1H, CH*H*Bn), 4.81 (dd, *J* = 10.8, 2.1 Hz, 2H, 2x CH*H*Bn), 4.72 – 4.59 (m, 3H, 3x CH*H*Bn), 4.51 – 4.41 (m, 2H, 2x CH*H*Bn), 4.13 (dt, *J* = 10.2, 5.1 Hz, 1H, H-1), 3.81 – 3.74 (m, 2H, H-2 H-3), 3.73 – 3.66 (m, 1H, H-6), 3.62 (td, *J* = 7.3, 3.5 Hz, 3H, H-4 H-5 H-6), 2.56 – 2.40 (m, 2H, CH_2-CH=CH_2). ^{13}C NMR (101 MHz, $CDCl_3$, HSQC, HMBC, HMBC-GATED) δ 138.9, 138.3, 138.29, 138.2 (C_q), 128.6, 128.6, 128.5, 128.3, 128.1, 128.1, 128.1, 128.0, 127.9, 127.1, 127.9, 127.8 (CH_{Arom}), 117.0 (CH_2-CH=CH_2), 82.5 (C-2/C-3), 80.2 (C-2/C-3), 78.2 (C-4/C-5), 75.6, 75.2 (CHBn), 73.8 (C-1), 73.6, 73.2 (CHBn), 71.2 (C-4/C-5), 69.0 (C-6), 29.9 (CH_2-C*H*=CH_2) HRMS (ESI) [M/Z]: [M + NH_4] calcd for $C_{37}NH_{44}O_5^+$ 582.3266 found 582.3217.

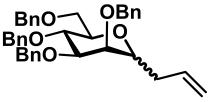

1-allyl-1-deoxy-2,3,4,6-tetra-*O*-benzyl-ᴅ-mannopyranoside (S2). The title compound was prepared according to the general glycosylation procedure, using mannose donor **2**[6] and allyl(chloro)dimethylsilane (0.023 mmol, 13 mg, 23%, >98:2, α:β) or allyltrimethylsilane (0.066 mmol, 37 mg, 66%, 72:28, α:β), yielding the title compound as a colorless oil. Spectral data for the α-anomer: ^{1}H NMR (400 MHz, $CDCl_3$, HH-COSY, HSQC, HMBC, HMBC-GATED) δ 7.41 – 7.23 (m, 20H, CH_{Arom}), 5.81 – 5.69 (m, 1H, CH_2-C*H*=CH_2), 5.05 – 5.02 (m, 2H, CH_2-CH=CH_2), 4.72 (t, *J* = 5.9 Hz, 1H, CHBn), 4.63 – 4.50 (m, 7H, 7x CHBn), 4.09 – 4.01 (m, 1H, H-1), 3.85 (m, *J* = 6.1 Hz, 2H, H-4 H-5), 3.80 – 3.75 (m, 2H, H-6 H-3), 3.73 – 3.68 (m, 1H, H-6), 3.62 (dd, *J* = 4.6, 3.0 Hz, 1H, H-2), 2.39 – 2.26 (m, 2H, CH_2-CH=CH_2). ^{13}C NMR (101 MHz, $CDCl_3$, HSQC, HMBC, HMBC-GATED) δ 134.5 (CH_2-*C*H=CH_2), 128.5, 128.5, 128.5, 128.4, 128.2, 128.1, 128.0, 127.9, 127.8, 127.8 (CH_{Arom}), 117.3 (CH_2-*C*H=CH_2), 77.0 (C-3), 75.3 (C-2), 75.0 (C-4), 74.0 (CH-Bn), 73.8 (C-5), 73.4 (CH-Bn), 72.5 (C-1), 72.2 (CHBn), 71.6 (CHBn), 69.3 (C-6), 29.8 (*C*H_2-CH=CH_2). HRMS (ESI) [M/Z]: [M + NH_4] calcd for $C_{37}NH_{44}O_5^+$ 582.3266 found 582.3210. Spectral data for the β-anomer: ^{1}H NMR (400 MHz, $CDCl_3$, HH-COSY, HSQC, HMBC, HMBC-GATED) δ 7.54 – 7.16 (m, 20H, CH_{Arom}), 5.81 – 5.62 (m, 1H, CH_2-C*H*=CH_2), 5.07 – 4.98 (m, 2H, CH_2-CH=CH_2), 4.87 (d, *J* = 10.7 Hz, 1H, CH*H*Bn), 4.81 – 4.71 (m, 2H, 2x CH*H*Bn), 4.70 – 4.63 (m, 2H, 2x CH*H*Bn), 4.62 – 4.51 (m, 3H, 3x CH*H*Bn), 3.95 – 3.85 (m, 1H, H-4), 3.79 (td, *J* = 3.3, 1.4 Hz, 1H, H-2), 3.76 (dd, *J* = 4.4, 1.9 Hz, 1H, H-6), 3.74 – 3.65 (m, 1H, H-6), 3.61 (dd, *J* = 9.5, 2.8 Hz, 1H, H-3), 3.46 (ddd, *J* = 9.7, 5.9, 1.9 Hz, 1H, H-5), 3.36 – 3.31 (m, 1H, H-1), 2.51 (dtt, *J* = 14.3, 6.4, 1.6 Hz, 1H, CH*H*-CH=CH_2), 2.38 – 2.25 (m, 1H, CH*H*-CH=CH_2). ^{13}C NMR (101 MHz, $CDCl_3$, HSQC, HMBC, HMBC-GATED) δ 138.9, 138.6, 138.4 (C_q), 134.8 (*C*H_2-CH=CH_2), 128.5, 128.5, 128.5, 128.4, 128.4, 128.1, 128.0, 127.8, 127.8, 127.6, 127.6 (CH_{Arom}), 117.4 (CH_2-CH=*C*H_2), 85.6 (C-3), 80.0 (C-5), 78.4 (C-1), 75.6 (C-4), 75.4 (CH_2Bn), 74.7 (C-2), 74.4, 73.7, 72.6, 72.5 (CH_2Bn), 69.8 (C-6), 35.8 (*C*H_2-CH=CH_2). HRMS (ESI) [M/Z]: [M + NH_4] calcd for $C_{37}NH_{44}O_5^+$ 582.3266 found 582.3212.

References

(1) Hansen, T.; van der Vorm, S.; Tugny, C.; Remmerswaal, W. A.; van Hengst, J. M. A.; van der Marel, G. A.; Codée, J. D. C. Stereoelectronic Effects in Glycosylation Reactions. In *Reference Module in Chemistry, Molecular Sciences and Chemical Engineering*; Elsevier, 2021.

(2) Adero, P. O.; Amarasekara, H.; Wen, P.; Bohé, L.; Crich, D. The Experimental Evidence in Support of Glycosylation Mechanisms at the S_N1–S_N2 Interface. *Chem. Rev.* **2018**, *118* (17), 8242–8284.

(3) Hettikankanamalage, A. A.; Lassfolk, R.; Ekholm, F. S.; Leino, R.; Crich, D. Mechanisms of Stereodirecting Participation and Ester Migration from Near and Far in Glycosylation and Related Reactions. *Chem. Rev.* **2020**, *120* (15), 7104–7151.

(4) Crich, D. En Route to the Transformation of Glycoscience: A Chemist's Perspective on Internal and External Crossroads in Glycochemistry. *J. Am. Chem. Soc.* **2021**, *143* (1), 17–34.

(5) Andreana, P. R.; Crich, D. Guidelines for *O*-Glycoside Formation from First Principles. *ACS Cent. Sci.* **2021**, *7* (9), 1454–1462.

(6) Hansen, T.; Lebedel, L.; Remmerswaal, W. A.; van der Vorm, S.; Wander, D. P. A.; Somers, M.; Overkleeft, H. S.; Filippov, D. V.; Désiré, J.; Mingot, A.; Bleriot, Y.; van der Marel, G. A.; Thibaudeau, S.; Codée, J. D. C. Defining the S_N1 Side of Glycosylation Reactions: Stereoselectivity of Glycopyranosyl Cations. *ACS Cent. Sci.* **2019**, *5* (5), 781–788.

(7) Hansen, T.; Elferink, H.; van Hengst, J. M. A.; Houthuijs, K. J.; Remmerswaal, W. A.; Kromm, A.; Berden, G.; van der Vorm, S.; Rijs, A. M.; Overkleeft, H. S.; Filippov, D. V.; Rutjes, F. P. J. T.; van der Marel, G. A.; Martens, J.; Oomens, J.; Codée, J. D. C.; Boltje, T. J. Characterization of Glycosyl Dioxolenium Ions and Their Role in Glycosylation Reactions. *Nat. Commun.* **2020**, *11* (1), 2664.

(8) Remmerswaal, W. A.; Elferink, H.; Houthuijs, K. J.; Hansen, T.; ter Braak, F.; Berden, G.; van der Vorm, S.; Martens, J.; Oomens, J.; van der Marel, G. A.; Boltje, T. J.; Codée, J. D. C. Anomeric Triflates versus Dioxanium Ions: Different Product-Forming Intermediates from 3-Acyl Benzylidene Mannosyl and Glucosyl Donors. *J. Org. Chem.* **2024**, *89* (3), 1618–1625.

(9) Remmerswaal, W. A.; Houthuijs, K. J.; van de Ven, R.; Elferink, H.; Hansen, T.; Berden, G.; Overkleeft, H. S.; van der Marel, G. A.; Rutjes, F. P. J. T.; Filippov, D. V.; Boltje, T. J.; Martens, J.; Oomens, J.; Codée, J. D. C. Stabilization of Glucosyl Dioxolenium Ions by "Dual Participation" of the 2,2-Dimethyl-2-(*Ortho*-Nitrophenyl)Acetyl (DMNPA) Protection Group for 1,2-*Cis*-Glucosylation. *J. Org. Chem.* **2022**, *87* (14), 9139–9147.

(10) Chun, Y.; Remmerswaal, W. A.; Codée, J. D. C.; Woerpel, K. A. Neighboring-Group Participation by C-2 Acyloxy Groups: Influence of the Nucleophile and Acyl Group on the Stereochemical Outcome of Acetal Substitution Reactions. *Chem. Eur. J.* **2023**, *29*, e202301894.

(11) Demkiw, K. M.; Remmerswaal, W. A.; Hansen, T.; van der Marel, G. A.; Codée, J. D. C.; Woerpel, K. A. Halogen Atom Participation in Guiding the Stereochemical Outcomes of Acetal Substitution Reactions. *Angew. Chem. Int. Ed.* **2022**, *61*, e202209401.

(12) Hengst, J. M. A. van; Hellemons, R. J. C.; Remmerswaal, W. A.; Vrande, K. N. A. van de; Hansen, T.; Vorm, S. van der; Overkleeft, H. S.; Marel, G. A. van der; Codée, J. D. C. Mapping the Effect of Configuration and Protecting Group Pattern on Glycosyl Acceptor Reactivity. *Chem. Sci.* **2023**, *14* (6), 1532–1542.
(13) Yang, M. T.; Woerpel, K. A. The Effect of Electrostatic Interactions on Conformational Equilibria of Multiply Substituted Tetrahydropyran Oxocarbenium Ions. *J. Org. Chem.* **2009**, *74* (2), 545–553.
(14) Ayala, L.; Lucero, C. G.; Romero, J. A. C.; Tabacco, S. A.; Woerpel, K. A. Stereochemistry of Nucleophilic Substitution Reactions Depending upon Substituent: Evidence for Electrostatic Stabilization of Pseudoaxial Conformers of Oxocarbenium Ions by Heteroatom Substituents. *J. Am. Chem. Soc.* **2003**, *125* (50), 15521–15528.
(15) Beaver, M. G.; Woerpel, K. A. Erosion of Stereochemical Control with Increasing Nucleophilicity: *O*-Glycosylation at the Diffusion Limit. *J. Org. Chem.* **2010**, *75* (4), 1107–1118.
(16) Kendale, J. C.; Valentín, E. M.; Woerpel, K. A. Solvent Effects in the Nucleophilic Substitutions of Tetrahydropyran Acetals Promoted by Trimethylsilyl Trifluoromethanesulfonate: Trichloroethylene as Solvent for Stereoselective *C*- and *O*-Glycosylations. *Org. Lett.* **2014**, *16* (14), 3684–3687.
(17) Krumper, J. R.; Salamant, W. A.; Woerpel, K. A. Correlations Between Nucleophilicities and Selectivities in the Substitutions of Tetrahydropyran Acetals. *J. Org. Chem.* **2009**, *74* (21), 8039–8050.
(18) Krumper, J. R.; Salamant, W. A.; Woerpel, K. A. Continuum of Mechanisms for Nucleophilic Substitutions of Cyclic Acetals. *Org. Lett.* **2008**, *10* (21), 4907–4910.
(19) Lucero, C. G.; Woerpel, K. A. Stereoselective C-Glycosylation Reactions of Pyranoses: The Conformational Preference and Reactions of the Mannosyl Cation. *J. Org. Chem.* **2006**, *71* (7), 2641–2647.
(20) Woods, R. J.; Andrews, C. W.; Bowen, J. P. Molecular Mechanical Investigations of the Properties of Oxocarbenium Ions. 2. Application to Glycoside Hydrolysis. *J. Am. Chem. Soc.* **1992**, *114* (3), 859–864.
(21) Woods, R. J. Computational Carbohydrate Chemistry: What Theoretical Methods Can Tell Us. *Glycoconj. J.* **1998**, *15* (3), 209–216.
(22) Whitfield, D. M. DFT Studies of the Ionization of Alpha and Beta Glycopyranosyl Donors. *Carbohydr. Res.* **2007**, *342* (12), 1726–1740.
(23) Whitfield, D. M. Plausible Transition States for Glycosylation Reactions. *Carbohydrate Research* **2012**, *356*, 180–190.
(24) Elferink, H.; Severijnen, M. E.; Martens, J.; Mensink, R. A.; Berden, G.; Oomens, J.; Rutjes, F. P. J. T.; Rijs, A. M.; Boltje, T. J. Direct Experimental Characterization of Glycosyl Cations by Infrared Ion Spectroscopy. *J. Am. Chem. Soc.* **2018**, *140* (19), 6034–6038.
(25) Merino, P.; Delso, I.; Pereira, S.; Orta, S.; Pedrón, M.; Tejero, T. Computational Evidence of Glycosyl Cations. *Org. Biomol. Chem.* **2021**, *19* (11), 2350–2365.
(26) Braak, F. ter; Elferink, H.; Houthuijs, K. J.; Oomens, J.; Martens, J.; Boltje, T. J. Characterization of Elusive Reaction Intermediates Using Infrared Ion Spectroscopy: Application to the Experimental Characterization of Glycosyl Cations. *Acc. Chem. Res.* **2022**, *55* (12), 1669–1679.
(27) Elferink, H.; Remmerswaal, W. A.; Houthuijs, K. J.; Jansen, O.; Hansen, T.; Rijs, A. M.; Berden, G.; Martens, J.; Oomens, J.; Codée, J. D. C.; Boltje, T. J. Competing C-4 and C-5-Acyl Stabilization of Uronic Acid Glycosyl Cations. *Chem. Eur. J.* **2022**, *28*, e202201724.
(28) Mucha, E.; Marianski, M.; Xu, F.-F.; Thomas, D. A.; Meijer, G.; von Helden, G.; Seeberger, P. H.; Pagel, K. Unravelling the Structure of Glycosyl Cations via Cold-Ion Infrared Spectroscopy. *Nat. Commun.* **2018**, *9* (1), 4174.
(29) Marianski, M.; Mucha, E.; Greis, K.; Moon, S.; Pardo, A.; Kirschbaum, C.; Thomas, D. A.; Meijer, G.; von Helden, G.; Gilmore, K.; Seeberger, P. H.; Pagel, K. Remote Participation during Glycosylation Reactions of Galactose Building Blocks: Direct Evidence from Cryogenic Vibrational Spectroscopy. *Angew. Chem. Int. Ed.* **2020**, *59* (15), 6166–6171.
(30) Greis, K.; Leichnitz, S.; Kirschbaum, C.; Chang, C.-W.; Lin, M.-H.; Meijer, G.; von Helden, G.; Seeberger, P. H.; Pagel, K. The Influence of the Electron Density in Acyl Protecting Groups on the Selectivity of Galactose Formation. *J. Am. Chem. Soc.* **2022**, *144* (44), 20258–20266.
(31) Whitfield, D. M. Chapter 4 Computational Studies of the Role of Glycopyranosyl Oxacarbenium Ions in Glycobiology and Glycochemistry. In *Advances in Carbohydrate Chemistry and Biochemistry*; Academic Press, 2009; Vol. 62, pp 83–159.
(32) Remmerswaal, W. A.; Hansen, T.; Hamlin, T. A.; Codée, J. D. C. Origin of Stereoselectivity in S_E2' Reactions of Six-Membered Ring Oxocarbenium Ions. *Chem. Eur. J.* **2023**, *29* (14), e202203490.
(33) Chun, Y.; Luu, K. B.; Woerpel, K. A. Acetal Substitution Reactions: Stereoelectronic Effects, Conformational Analysis, Reactivity vs Selectivity, and Neighboring-Group Participation. *Synlett* **2024**.
(34) Crich, D.; Sharma, I. Is Donor–Acceptor Hydrogen Bonding Necessary for 4,6-*O*-Benzylidene-Directed β-Mannopyranosylation? Stereoselective Synthesis of β-*C*-Mannopyranosides and α-*C*-Glucopyranosides. *Org. Lett.* **2008**, *10* (21), 4731–4734.
(35) McGarvey, G. J.; LeClair, C. A.; Schmidtmann, B. A. Studies on the Stereoselective Synthesis of C-Allyl Glycosides. *Org. Lett.* **2008**, *10* (21), 4727–4730.
(36) Mayr, H.; Kempf, B.; Ofial, A. R. π-Nucleophilicity in Carbon–Carbon Bond-Forming Reactions. *Acc. Chem. Res.* **2003**, *36* (1), 66–77.

(37) Ammer, J.; Nolte, C.; Mayr, H. Free Energy Relationships for Reactions of Substituted Benzhydrylium Ions: From Enthalpy over Entropy to Diffusion Control. *J. Am. Chem. Soc.* **2012**, *134* (33), 13902–13911.
(38) Previous research has indicated that the substitution of benzyl groups for methyl groups is computationally valid. The methyl and benzyl groups are sterically quite similar and generally yield similar computational results.
(39) Hansen, T. Glycosyl Cations in Glycosylation Reactions, Leiden University, 2020. https://hdl.handle.net/1887/138249 (accessed 2023-11-14).
(40) Madern, J. M.; Hansen, T.; van Rijssel, E. R.; Kistemaker, H. A. V.; van der Vorm, S.; Overkleeft, H. S.; van der Marel, G. A.; Filippov, D. V.; Codée, J. D. C. Synthesis, Reactivity, and Stereoselectivity of 4-Thiofuranosides. *J. Org. Chem.* **2019**, *84* (3), 1218–1227.
(41) The TS-α-$^{0}S_{2}$ transition states for both glycosyl cations could not be identified by conventional means due to electronic instability of the associated reactant complexes. As a representative structure for the transition state geometry, the point on the associated constrained potential energy surface with a similar C•••Si bond stretch as the TS-α-$^{4}C_{1}$ was selected. Supplementary Figures S1 and S2 contain diagrams which contain the Δ*E* along the reaction coordinate of each reaction pathway, demonstrating how this representative structure was selected. To demonstrate the effectiveness of this method, the reaction profiles between the glycosyl cations and allyltrichlorosilane were computed. For this weaker nucleophile the TS-α-$^{0}S_{2}$ transition states are clearly defined. In Supplementary Figures S3 and S4, it can be observed how the TS-α-$^{0}S_{2}$ barrier height compares with the other reaction paths.
(42) Legault, C. Y. CYLview, 1.0b, Université de Sherbrooke, 2009. http://www.cylview.org.
(43) The formed $SiMe_3^+$ cation eventually reacts with a triflate anion to form Tf_2OSiMe_3.
(44) To confirm this, the HOMO energy of the nucleophiles was computed, and indeed it is found that the HOMO energy of allyl(chloro)dimethylsilane (–6.966) is lower than that of allyltrimethylsilane (–6.597).
(45) Bickelhaupt, F. Understanding Reactivity with Kohn–Sham Molecular Orbital Theory: E2–S_N2 Mechanistic Spectrum and Other Concepts. *J. Comput. Chem.* **1999**, *20*, 114–128.
(46) Vermeeren, P.; van der Lubbe, S. C. C.; Fonseca Guerra, C.; Bickelhaupt, F. M.; Hamlin, T. A. Understanding Chemical Reactivity Using the Activation Strain Model. *Nat. Protoc.* **2020**, *15* (2), 649–667.
(47) Bickelhaupt, F. M.; Houk, K. N. Analyzing Reaction Rates with the Distortion/Interaction-Activation Strain Model. *Angew. Chem. Int. Ed.* **2017**, *56* (34), 10070–10086.
(48) Bickelhaupt, F. M.; Houk, K. N. Das Distortion/Interaction-Activation-Strain-Modell zur Analyse von Reaktionsgeschwindigkeiten. *Angew. Chem.* **2017**, *129* (34), 10204–10221.
(49) Currently, there are no methodologies available to decompose solvated interaction energy.
(50) Hansen, T.; Vermeeren, P.; Haim, A.; van Dorp, M. J. H.; Codée, J. D. C.; Bickelhaupt, F. M.; Hamlin, T. A. Regioselectivity of Epoxide Ring-Openings via S_N2 Reactions Under Basic and Acidic Conditions. *Eur. J. Org. Chem.* **2020**, *2020* (25), 3822–3828.
(51) Hansen, T.; Sun, X.; Dalla Tiezza, M.; van Zeist, W.-J.; van Stralen, J. N. P.; Geerke, D. P.; Wolters, L. P.; Poater, J.; Hamlin, T. A.; Bickelhaupt, F. M. C–X Bond Activation by Palladium: Steric Shielding versus Steric Attraction. *Chem. Eur. J.* **2022**, *28* (44), e202201093.
(52) The analysis with EDA at a consistent C1•••C_{allyl} bond distance is very insightful because all points exist on the potential energy surface. The validity of this approach was confirmed with a numerical experiment, in which double consistent geometry structures of all transition states were constructed and analyzed with ASM and EDA (Supplementary Figure S15). See the computational methods for details on the generation of the geometries.
(53) From the EDA analysis of double consistent geometries, it can be seen the interaction energy is lower for the glucosyl TS-α-$^{1}S_{3}$ consistent geometry, resulting from more stabilizing orbital interactions for the glucosyl TS-α-$^{4}C_{1}$ consistent geometry as the main contributor for this difference (Supplementary Figure S15).
(54) Note that steric repulsion between the reactants can manifest in both: (i) the strain energy, because steric repulsion deforms the fragments (*i.e.*, reactants), and (ii) the steric (Pauli) repulsion found in the nucleophile–electrophile interaction.
(55) From the EDA analysis of double consistent geometries, it can be seen the interaction energy is lower for the mannosyl TS-α-$^{0}S_{2}$ consistent geometry, resulting from increased destabilizing Pauli repulsion for the mannosyl TS-β-$^{1}C_{4}$ consistent geometry is the main contributor for this difference (Supplementary Figure S15).
(56) This can be seen from the glucosyl cation LUMO energies, which in the pathway leading to TS-α-$^{4}C_{1}$ is lower all along to reaction coordinate and drops more steeply as compared with the TS-α-$^{0}S_{2}$ (Supplementary Figure S14b).
(57) From the EDA analysis of double consistent geometries, it can be seen the interaction energy is lower for the mannosyl TS-α-$^{0}S_{2}$ consistent geometry, resulting from increased destabilizing Pauli repulsion for the mannosyl TS-α-$^{4}C_{1}$ consistent geometry as the main contributor for this difference (Supplementary Figure S15).
(58) Ardèvol, A.; Rovira, C. Reaction Mechanisms in Carbohydrate-Active Enzymes: Glycoside Hydrolases and Glycosyltransferases. Insights from Ab Initio Quantum Mechanics/Molecular Mechanics Dynamic Simulations. *J. Am. Chem. Soc.* **2015**, *137* (24), 7528–7547.

(59) Frisch, M. J.; Trucks, G. W.; Cheeseman, J. R.; Scalmani, G.; Caricato, M.; Hratchian, H. P.; Li, X.; Barone, V.; Bloino, J.; Zheng, G.; Vreven, T.; Montgomery, J. A.; Petersson, G. A.; Scuseria, G. E.; Schlegel, H. B.; Nakatsuji, H.; Izmaylov, A. F.; Martin, R. L.; Sonnenberg, J. L.; Peralta, J. E.; Heyd, J. J.; Brothers, E.; Ogliaro, F.; Bearpark, M.; Robb, M. A.; Mennucci, B.; Kudin, K. N.; Staroverov, V. N.; Kobayashi, R.; Normand, J.; Rendell, A.; Gomperts, R.; Zakrzewski, V. G.; Hada, M.; Ehara, M.; Toyota, K.; Fukuda, R.; Hasegawa, J.; Ishida, M.; Nakajima, T.; Honda, Y.; Kitao, O.; Nakai, H. Gaussian 09 Rev. D.01, 2009.

(60) Becke, A. D. Density-functional Thermochemistry. III. The Role of Exact Exchange. *J. Chem. Phys.* **1993**, *98* (7), 5648–5652.

(61) Lee, C.; Yang, W.; Parr, R. G. Development of the Colle-Salvetti Correlation-Energy Formula into a Functional of the Electron Density. *Phys. Rev. B Condens. Matter* **1988**, *37* (2), 785–789.

(62) Vosko, S. H.; Wilk, L.; Nusair, M. Accurate Spin-Dependent Electron Liquid Correlation Energies for Local Spin Density Calculations: A Critical Analysis. *Can. J. Phys.* **1980**, *58* (8), 1200–1211.

(63) Ditchfield, R.; Hehre, W. J.; Pople, J. A. Self-Consistent Molecular-Orbital Methods. IX. An Extended Gaussian-Type Basis for Molecular-Orbital Studies of Organic Molecules. *J. Chem. Phys.* **1971**, *54* (2), 724–728.

(64) Bootsma, A. N.; Wheeler, S. Popular Integration Grids Can Result in Large Errors in DFT-Computed Free Energies. ChemRxiv July 29, 2019.

(65) Sun, X.; Soini, T. M.; Poater, J.; Hamlin, T. A.; Bickelhaupt, F. M. PyFrag 2019—Automating the Exploration and Analysis of Reaction Mechanisms. *J. Comput. Chem.* **2019**, *40* (25), 2227–2233.

(66) Ribeiro, R. F.; Marenich, A. V.; Cramer, C. J.; Truhlar, D. G. Use of Solution-Phase Vibrational Frequencies in Continuum Models for the Free Energy of Solvation. *J. Phys. Chem. B* **2011**, *115* (49), 14556–14562.

(67) Luchini, G.; Alegre-Requena, J. V.; Funes-Ardoiz, I.; Paton, R. S. GoodVibes: Automated Thermochemistry for Heterogeneous Computational Chemistry Data. *F1000Res* **2020**, *9*, 291.

(68) Beek, B. van; Bochove, M. A. van; Hamlin, T. A.; Bickelhaupt, F. M. Nucleophilic Substitution at Di- and Triphosphates: Leaving Group Ability of Phosphate versus Diphosphate. *Electron. Struct.* **2019**, *1* (2), 024001.

(69) Vermeeren, P.; Hansen, T.; Jansen, P.; Swart, M.; Hamlin, T. A.; Bickelhaupt, F. M. A Unified Framework for Understanding Nucleophilicity and Protophilicity in the S_N2/E2 Competition. *Chem. Eur. J.* **2020**, *26* (67), 15538–15548.

(70) Galabov, B.; Koleva, G.; Schaefer III, H. F.; Allen, W. D. Nucleophilic Influences and Origin of the S_N2 Allylic Effect. *Chem. Eur. J.* **2018**, *24* (45), 11637–11648.

(71) Hansen, T.; Vermeeren, P.; Yoshisada, R.; Filippov, D. V.; van der Marel, G. A.; Codée, J. D. C.; Hamlin, T. A. How Lewis Acids Catalyze Ring-Openings of Cyclohexene Oxide. *J. Org. Chem.* **2021**, *86* (4), 3565–3573.

(72) Hansen, T.; Vermeeren, P.; Bickelhaupt, F. M.; Hamlin, T. A. Origin of the α-Effect in S_N2 Reactions. *Angew. Chem. Int. Ed.* **2021**, *60* (38), 20840–20848.

(73) Hansen, T.; Roozee, J. C.; Bickelhaupt, F. M.; Hamlin, T. A. How Solvation Influences the S_N2 versus E2 Competition. *J. Org. Chem.* **2022**, *87* (3), 1805–1813.

(74) Bickelhaupt, F. M.; Baerends, E. J. Kohn-Sham Density Functional Theory: Predicting and Understanding Chemistry. In *Reviews in Computational Chemistry*; John Wiley & Sons, Ltd: New York, 2000; pp 1–86.

(75) Velde, G. te; Bickelhaupt, F. M.; Baerends, E. J.; Guerra, C. F.; Gisbergen, S. J. A. van; Snijders, J. G.; Ziegler, T. Chemistry with ADF. *Journal of Computational Chemistry* **2001**, *22* (9), 931–967.

(76) Fonseca Guerra, C.; Snijders, J. G.; te Velde, G.; Baerends, E. J. Towards an Order-*N* DFT Method. *Theor Chem Acc* **1998**, *99* (6), 391–403.

(77) ADF2018, SCM, Theoretical Chemistry, Vrije Universiteit, Amsterdam, The Netherlands, https://www.scm.com.

(78) Van Lenthe, E.; Baerends, E. J. Optimized Slater-Type Basis Sets for the Elements 1–118. *J. Comput. Chem.* **2003**, *24* (9), 1142–1156.

(79) Franchini, M.; Philipsen, P. H. T.; Visscher, L. The Becke Fuzzy Cells Integration Scheme in the Amsterdam Density Functional Program Suite. *J. Comput. Chem.* **2013**, *34* (21), 1819–1827.

(80) Franchini, M.; Philipsen, P. H. T.; van Lenthe, E.; Visscher, L. Accurate Coulomb Potentials for Periodic and Molecular Systems through Density Fitting. *J. Chem. Theory Comput.* **2014**, *10* (5), 1994–2004.

(81) Lenthe, E. van; Baerends, E. J.; Snijders, J. G. Relativistic Regular Two-component Hamiltonians. *J. Chem. Phys.* **1993**, *99* (6), 4597–4610.

(82) van Lenthe, E.; Baerends, E. J.; Snijders, J. G. Relativistic Total Energy Using Regular Approximations. *J. Chem. Phys.* **1994**, *101* (11), 9783–9792.